Bandgap analysis of periodic composite plates considering fluid–structure coupling

Runze Zhang, Yu Cong, M. Sellam, Amer Chpoun

Bandgap analysis of periodic composite plates considering fluid-structure coupling

R. Z. Zhang [a], **Y. Cong** [a], **M. Sellam** [a], **A. Chpoun** [a].

[a] *Université Paris-Saclay, Univ Evry, LMEE, 91020, Evry, France*

Abstract

This article presents a novel approach for predicting vibration bandgaps in periodic composite plates with fluid-structure interaction (FSI) using a unit cell-based finite element model. The novelty of our approach lies in the formulation of a fluid-induced added mass matrix, which integrates the Bloch periodic boundary condition, allowing for the incorporation of the fluid's inertial effect in the context of unit cell-based bandgap analysis. We therefore construct a unit cell model comprising a composite Mindlin plate which integrates periodic FSI effects with the simultaneous application of Bloch conditions on both the structure and the fluid domains. Subsequently, we studied a set of periodic composite plates with FSI effects on one or both sides, thereby assessing the influence of the fluid properties such as density and the fluid domain dimension on the structure vibration. The bandgap prediction is compared with the frequency response simulations which involve diversified microstructure designs. The obtained results provide indications regarding the effectiveness and applicability of the proposed numerical methodology.

Keywords: Fluid-structure interaction; Bloch boundary condition; Vibration bandgap; Mindlin plate

1 Introduction

Periodic composite plates hold significant relevance in both civil and engineering applications. Due to their structural characteristics, such as the weak inertia across the thickness, their vibration behaviour can be significantly influenced by fluid-structure interaction (FSI). Therefore, accurately modelling the FSI effect is important in designing periodic composite structures to achieve desired wave propagation properties [1, 2, 3], including vibration bandgaps and dispersion [4, 5]. This necessity is particularly significant in fields which require tunable wave propagation properties, such as aerospace [6], vehicle [7], marine structures [8], and turbo machine components [9].

While low-density airflow typically has minimal FSI effects, the presence of denser fluids, such as liquids, requires particular consideration of FSI conditions to account for their influence on the structure vibration. Various FSI coupled systems have been developed using finite element modelling [10, 11] to address different fluid conditions. For scenarios involving the pure inertial effects of the fluid on the structure, the method of effective added mass has been widely adopted [12, 13]. This approach calculates

Corresponding authors:
runze.zhang@univ-evry.fr (R. Z. Zhang).

Accepted by Journal of Sound and Vibration
03/2024

the additional mass induced by the surrounding incompressible fluid environment and integrates its inertia into the structural dynamics equations, considering displacement and pressure fields for the structure and the fluid domains, respectively. In situations with more complex fluid conditions, such as hydro-elastic problems and structural-acoustic problems, coupled FSI systems have been proposed to account for fluid gravity and compressibility conditions [14], respectively. These methods, initially resolved as non-symmetric coupled systems based on classical kinematic descriptions, have evolved to include symmetric equivalents using additional degrees of freedom (DOFs) like fluid displacement and velocity potentials [15, 16]. Subsequently, these FSI models have been successfully applied to academic and engineering structures [17, 18, 19]. However, in the context of designing periodic plate structures, further adaptation is necessary to incorporate periodic boundary conditions into the description of the FSI coupled system, as required for vibration analysis that is performed based on unit cell calculations.

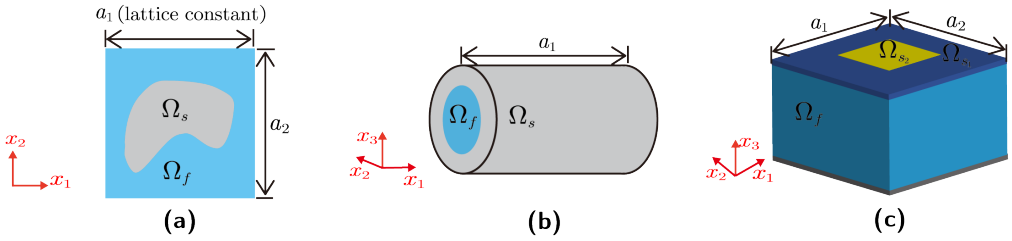

Figure 1: Unit cells involving FSI of (a) solid/fluid phonic crystals, (b) periodic composite liquid-filled pipe and (c) periodic composite plate in contact with fluids.

The unit cell model serves as a fundamental tool for describing the periodic microstructure of composite plates within their fluid environments, allowing for the prediction of their global vibroacoustic behaviours and enabling optimal design. This approach requires the incorporation of periodic boundary conditions on the unit cell model, using the Bloch-Floquet theorem [20]. While this methodology has been extensively utilised for the design of general periodic structure dynamics, its extension to the FSI context requires further investigation depending on the specific fluid-structure architecture. Existing literature has explored unit cell architectures depicted in Figures 1(a) and (b). In the former [18] [21] [22], Bloch boundary conditions are implemented solely on the fluid domain, given the periodic arrangement of the structure within the fluid domain, as shown in Figure 1(a). In the latter scenario [23] [24] [25], periodic conditions are applied to both the structure and fluid domains. The technique is particularly suited for tubular structures with interior fluid environment, as depicted in Figure 1(b). However, for immersed planar composite structures, as in the present study, prior research has solely focused on implementing periodic conditions on the boundaries of the structure domain [26]. Furthermore, while analytical model [27] adopting plane wave expansion (PWE) and hybrid modelling approach [28] combining semi-analytical PWE and finite element modelling have been explored, a comprehensive finite element-based unit cell model that integrates Bloch boundary conditions on both the fluid and solid domains, as depicted in Figure 1(c), remains to be explored. Such an architecture holds significant potential for a wide range of applications involving the vibration control of underwater thin-walled structures.

In this context, we propose a modelling approach that involves calculating the effective added-mass matrix through unit cell calculations with Bloch periodic conditions applied to both the structure and fluid boundaries. This added mass calculation integrates the effect of fluid inertia on the composite

plate from one or both of its adjacent surfaces. Specifically, the composite structure is modeled using 4-node Mindlin plate finite elements [29], while the fluid dynamics is represented using hexahedral solid elements. The fluid-structure interface is modeled by a consistent discretization comprising 4-node planar elements. Subsequently, a FSI matrix is computed by integrating over the fluid-structure interface, connecting the displacement DOFs of the structure domain to the pressure DOFs of the fluid domain. This unit cell model enables the prediction of vibration bandgaps for which dispersive band structures have been studied.

Following the development of the unit cell design, its evaluation with respect to the associated full-scale composite plate model can be conducted using experimental, analytical, or numerical techniques. Experimental methods, such as ultrasonic transmission [30], provide insights into bandgaps in two-dimensional periodic composites within ultrasonic frequency ranges. Analytical evaluations often employ the PWE method [31], which, while effective, can be challenging for general applications involving complex structures due to the required effort in analytical integration over the heterogeneous material boundaries. In this study, we compare the bandgap predictions of the unit cell design with the associated full-scale models using a numerical model based on frequency response function (FRF) analysis [32]. By calculating and comparing the frequency responses of the full-scale composite plate with the bandgap predictions, it shows that the proposed numerical methodology is practicable and versatile.

The paper is organised to present the theory, numerical implementation, and the achieved results of the proposed bandgap analysis approach with FSI effect. Section 2 will present the variational formulation of the FSI coupled system concerning wave propagation. Following that, Section 3 will introduce the finite element formulation of the general coupled system. Subsequently, Section 4 will provide details on the finite element implementation of the coupled system composed of periodic composite Mindlin plates and the acoustic fluid models, followed by the unit cell model incorporating Bloch-Floquet boundary conditions. In Section 5, the approach will be applied to three groups of numerical cases, starting with an investigation into the impact of FSI effects on the vibration and wave propagation characteristics of the composite immersed in a fluid environment, first on one side and then on both sides. Comparison results will be presented based on frequency response simulations. Finally, Section 6 will offer concluding remarks.

2 Elastodynamics of fluid-structure coupled system

In this section, we describe the variational formulations of the wave propagation problem within the fluid-structure interaction (FSI) context. We start by presenting the equilibrium equations for the wave propagation problem in the solid domain, followed by the fluid domain. Then, by establishing the equilibrium at the fluid-structure interface, we deduce the equilibrium equations for the fluid-structure interaction problem within the context of linear oscillations.

2.1 Equations of motion of the solid domain

We use Ω_s to denote the spatial domain occupied by the solid, and $\mathbf{u}$ the displacement vector of a point $\mathbf{x}(x_1, x_2, x_3) \in \Omega_s$ at a given time instant t. The components of $\mathbf{u}$ in the Cartesian coordinates (x_1, x_2, x_3) are u_1, u_2, and u_3. Disregarding body forces, the vibration of Ω_s can be described by $\mathbf{u}$,

which satisfies the elastodynamic equation:

$$\rho_s \frac{\partial^2 \mathbf{u}}{\partial t^2} - \nabla \cdot \boldsymbol{\sigma} = 0, \quad \text{in } \Omega_s. \tag{1}$$

This equation describes the equilibrium between the inertial and elastic forces. It can be obtained from d'Alembert's wave equation under the assumption of homogeneous material and linear vibrations with respect to the equilibrium state. In Eq. (1), ρ_s denotes the solid density, and $\boldsymbol{\sigma}$ represents the Cauchy stress tensor, which is given by the constitutive relation:

$$\boldsymbol{\sigma} = \mathbb{C} : \boldsymbol{\varepsilon}. \tag{2}$$

Under the condition of linear vibrations, infinitesimal transformation can be applied. The fourth-order elasticity tensor $\mathbb{C}$ involved in the constitutive relation Eq. (2) can be expressed using the matrix expression in Cartesian coordinates (x_1, x_2, x_3) provided in Appendix A. Then, $\boldsymbol{\varepsilon}$ denotes the Cauchy strain, whose components are obtained from the displacement field by considering first-order terms as:

$$\boldsymbol{\varepsilon} = \frac{1}{2}\left[\nabla \mathbf{u} + (\nabla \mathbf{u})^{\mathrm{T}}\right] . \tag{3}$$

The equilibrium Eq. (1) for the solid domain Ω_s is supplemented by the mechanical boundary conditions as follows:

$$\begin{aligned} \mathbf{u} &= 0 \quad \text{on } \Gamma_{su} \\ \boldsymbol{\sigma} \cdot \mathbf{n}^s &= 0 \quad \text{on } \Gamma_{s\sigma} \end{aligned} , \tag{4}$$

where Γ_{su} and $\Gamma_{s\sigma}$ represent the boundaries of Ω_s, on which displacement and stress boundary conditions are considered, respectively. $\mathbf{n}^s$ is the normal vector on the solid boundaries.

2.2 Wave equation of the fluid domain

Let Ω_f denote the fluid domain and (x_1, x_2, x_3) the Cartesian coordinates in which the kinematics of material points that belong to Ω_f are expressed. The governing equation for acoustic wave propagation in Ω_f can be formulated in terms of the pressure fluctuation $p(\mathbf{x})$ at a point $\mathbf{x}$ relative to the fluid's steady state . Considering a non-viscous, compressible fluid initially at rest and neglecting body forces, we can describe the fluid dynamics using the d'Alembert's wave equation with respect to the pressure:

$$\frac{1}{c_0^2}\frac{\partial^2 p}{\partial t^2} - \nabla \cdot \nabla p = 0, \quad \text{in } \Omega_f, \tag{5}$$

where c_0 denotes the speed of sound in the fluid under consideration. Analogous to Eq. (1), Eq. (5) incorporates second-order derivatives with respect to time and space. However, for dense and weakly compressible fluids, such as liquids, the fluctuation of fluid density with respect to the steady state density ($\rho_0 = \rho_f$) is often neglected, i.e. $\rho(\mathbf{x}) = 0$. Then the mass and momentum conservation becomes:

$$\frac{\partial \rho}{\partial t} + \rho_f \nabla \cdot \mathbf{v} = 0 + \rho_f \nabla \cdot \mathbf{v} = 0, \quad \text{in } \Omega_f, \tag{6}$$

$$\rho_f \frac{\partial \mathbf{v}}{\partial t} + \nabla p = 0, \quad \text{in } \Omega_f, \tag{7}$$

where $\mathbf{v}$ represents the fluctuation of fluid velocity. Subsequently, we substitute the time derivative into Eq. 6 and the spatial derivative into Eq. 7, and combine the two equations, resulting in the governing equation for the pressure fluctuation in Ω_f, the liquid-filled domain, in the form of the Laplace equation:

$$\nabla \cdot \nabla p = 0, \quad \text{in } \Omega_f, \tag{8}$$

which conforms to the Laplace equation. Therefore, the vibration of Ω_f, considering non-viscous and incompressible fluids, which we focus on in this work, can be described by the following problem, comprising the governing equation Eq. (8), supplemented by the boundary conditions regarding the pressure and its variation on the free and fixed boundaries, which writes:

$$\begin{array}{cc} p = 0 & \text{on } \Gamma_{f0} \\ \nabla p \cdot \mathbf{n}^f = 0 & \text{on } \Gamma_{f\pi} \end{array}, \tag{9}$$

where Γ_{f0} and $\Gamma_{f\pi}$ refer to the free and fixed boundaries of the fluid domain, respectively. $\mathbf{n}^f$ is the normal vector on the fluid boundaries. It is worth noting that the assumptions made for the non-viscous, incompressible fluid do not prevent the formulation from being applied in practice to liquid flows with low or negligible velocities, corresponding to laminar flow conditions.

2.3 Equilibrium on the fluid-structure interface

Coupling between the fluid domain Ω_f and the solid domain Ω_s is described by the equilibrium conditions established at the fluid-structure interface Γ (see Figure 2). These conditions ensure the continuity of the normal components of the stress tensor and the acceleration field. The first condition arises from the action of the fluid on the solid. Specifically, the fluid exerts forces on the solid in the direction normal to the fluid-structure interface. This leads to the following condition:

$$\boldsymbol{\sigma} \cdot \mathbf{n}^s = p\mathbf{n}, \quad \text{on } \Gamma, \tag{10}$$

where $\mathbf{n}$ is the normal vector at the fluid-structure interface. In this work, we adopt the convention that the normal vector $\mathbf{n}$ points from Ω_f towards Ω_s.

Conversely, the second equilibrium condition results from the action of the solid on the fluid. The solid domain imposes its acceleration onto the fluid through the fluid-structure interface, again in the direction normal to the interface. Thus, the continuity of acceleration yields:

$$\nabla p \cdot \mathbf{n} = -\rho_f \ddot{\mathbf{u}} \cdot \mathbf{n}, \quad \text{on } \Gamma, \tag{11}$$

where ρ_f refers to the fluid density. Eq. (10) and Eq. (11) establish the mutual effect between the solid and fluid domains by balancing forces and accelerations at the interface. This balance is expressed as function of the mechanical displacement $\mathbf{u}$, and the fluid pressure fluctuation p, and characterises the dynamics of the fluid-structure interaction problem.

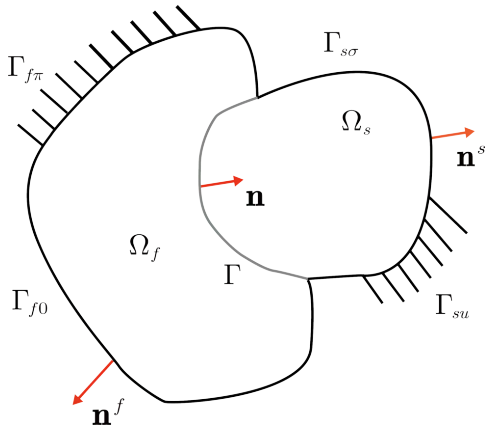

Figure 2: The general FSI problem representation.

2.4 Weak formulation of the coupled problem

Focusing on the equilibrium of the solid domain Ω_s, its dynamics is dictated by the governing equation given by Eq. (1), under the influence of the boundary conditions (Eq. (10)) exerted via the fluid-structure interface Γ. Utilising the variational method, we assign a virtual displacement, denoted by $\delta\mathbf{u}$, and a virtual pressure fluctuation, represented by δp, which are multiplied with Eq. (1) and Eq. (10). We then proceed with integration over the respective domain using Green's formula, and obtain the integral form of the elastodynamic equation of the solid domain that accounts for the effects of fluid-structure interaction, as expressed in Eq. (12).

$$\int_{\Omega_s} \rho_s \ddot{\mathbf{u}} \cdot \delta\mathbf{u} \, \mathrm{d}\Omega + \int_{\Omega_s} \boldsymbol{\sigma} : \delta\boldsymbol{\varepsilon} \, \mathrm{d}\Omega_s = \int_{\Gamma} p\mathbf{n} \cdot \delta\mathbf{u} \, \mathrm{d}\Gamma. \tag{12}$$

Correspondingly, the dynamic behaviour of the fluid domain Ω_f is described by its governing equation (Eq. (8)) under the influence of the boundary conditions given by Eq. (11). Adopting a similar approach as for Eq. (12), we apply the variational method on Eq. (8) and Eq. (11), and subsequently acquire the integral expression of the elastodynamic equation for the fluid domain involving the fluid-structure interaction, as stated in Eq. (13).

$$\int_{\Omega_f} \nabla p \cdot \nabla \delta p \, \mathrm{d}\Omega_f = -\rho_f \int_{\Gamma} \ddot{\mathbf{u}} \cdot \mathbf{n} \delta p \, \mathrm{d}\Gamma. \tag{13}$$

The set of equations, Eq. (12) and Eq. (13), constitutes the governing equation system that dictates the elastodynamic behaviour of the fluid-structure interaction problem. This system involves the behaviour of both the solid domain Ω_s and the fluid domain Ω_f, integrating the account for their interactions in terms of pressure forces and accelerations across the interface Γ. In subsequent sections, the focus will move to the resolution of this system using a discretisation approach for Ω_s based on a 4-node plate finite element with 12 degrees of freedom, and for Ω_f employing classical 8-node hexahedral elements. Particular attention will be placed on the treatment of the interface Γ that interconnects Ω_s and Ω_f.

3 FSI interface implementation

With the variational formulation of the FSI system obtained in Section 2, we focus here on its finite element implementation. The FSI system comprises a solid domain Ω_s, represented by Mindlin plate finite elements, a fluid domain Ω_f, modeled using 8-node hexahedral elements, and an interface domain Γ. Appendices A and B offer details on the finite element implementation of the solid and fluid domains, respectively. We present particularly the implementation of the interface domain, with emphasise on the integration of Bloch boundary conditions within the periodic unit cell model.

3.1 Fluid-structure coupling: interface finite element modelling

The dynamic behaviour of both Ω_s and Ω_f is defined by their respective governing equations (Eq. (12) and Eq. (13)) and influenced by the corresponding boundary conditions applied via the fluid-structure interface Γ. These boundary conditions are expressed as pressure forces and accelerations that act across the interface Γ, following the direction of the normal vector $\mathbf{n}$ perpendicular to Γ. These interactions emerge from the reciprocal actions between the fluid and solid domains. Specifically, they involve the application of pressure forces from the fluid onto the solid and, conversely, the imposition of accelerations on the fluid due to the dynamic behaviour of the solid. These boundary conditions are manifested as the right-hand side terms in the equilibrium equations (Eq. (12, 13)) of both the solid and fluid domains.

To illustrate the finite element implementation of these equations, let us consider a general scenario where an infinite plate is in contact with an infinite liquid fluid medium by its one side, as illustrated in Figure 3(a). The fluid's properties comply with the assumptions presented in Section 6. As for demonstration, we have the homogeneous plate extends infinitely far away in four directions (including $+\boldsymbol{x}_1$, $-\boldsymbol{x}_1$, $+\boldsymbol{x}_2$, $-\boldsymbol{x}_2$), and the ideal liquid fluid medium is also unlimited in five directions (including $+\boldsymbol{x}_1$, $-\boldsymbol{x}_1$, $+\boldsymbol{x}_2$, $-\boldsymbol{x}_2$, $-\boldsymbol{x}_3$). The displacement field within the solid domain using the mindlin plate assumption will vary spatially according to the (x_1, x_2) coordinates. The pressure fluctuation within the fluid domain is assumed to vary spatially according to the (x_1, x_2, x_3) coordinates.

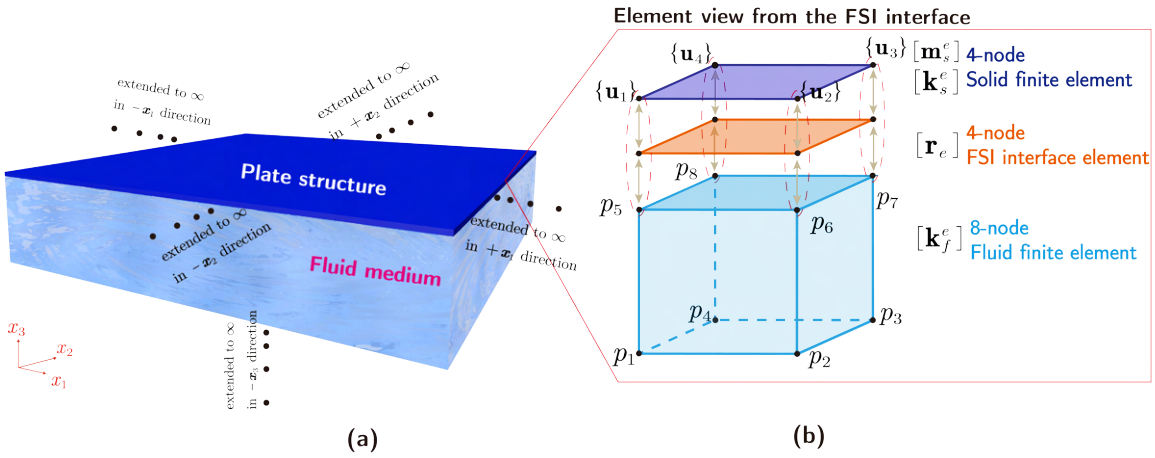

Figure 3: Example of a plate in contact with a fluid medium by one side, and the associated interface finite element model: (a) the FSI system (b) and associated interface finite element model.

Discretisation of the interface: The interface Γ between the plate the fluid medium is modelled by classical 4-node quadrilateral finite elements, but the discretisation of Γ requires particular consideration. In this work, the solid and fluid domains, Ω_s and Ω_f, along with the interface Γ, are discretised using separate but conforming meshes. This means that although the upper surface of the fluid domain, the plate model, and their interface are discretised independently, the meshes share common nodes, as depicted in Figure 3(b).

Interactions between Ω_s and Ω_f are defined by their respective boundary conditions applied on Γ. This signifies that both the field of kinematics variables $\{\mathbf{u}\}$ associated with Ω_s, and the field of pressure fluctuation $\{\mathbf{p}\}$ from Ω_f, need to be approximated on the interface. Consequently, the chosen 4-node quadrilateral finite element for discretising Γ should allow for the approximation of both $\{\mathbf{u}\}$ and $\{\mathbf{p}\}$. Therefore, we construct the interpolation matrix $[\mathbf{N}_{\Gamma s}]$ as follows:

$$[\mathbf{N}_{\Gamma s}] = \begin{bmatrix} N_{\Gamma 1} & 0 & 0 & & N_{\Gamma 4} & 0 & 0 \\ 0 & N_{\Gamma 1} & 0 & \cdots & 0 & N_{\Gamma 4} & 0 \\ 0 & 0 & N_{\Gamma 1} & & 0 & 0 & N_{\Gamma 4} \end{bmatrix} \quad , \tag{14}$$

for the interpolation of $\{\mathbf{u}\}$, with $\{\mathbf{u}_e\} = [\mathbf{N}_{\Gamma s}]\{\mathbf{u}\}$. Meanwhile, we construct a second interpolation matrix $[\mathbf{N}_{\Gamma f}]$ as:

$$[\mathbf{N}_{\Gamma f}] = \begin{bmatrix} N_{\Gamma 1} & N_{\Gamma 2} & N_{\Gamma 3} & N_{\Gamma 4} \end{bmatrix} \quad , \tag{15}$$

for the interpolation of $\{\mathbf{p}\}$, where $p_e = [\mathbf{N}_{\Gamma f}]\{\mathbf{p}\}$. Notably, both $[\mathbf{N}_{\Gamma s}]$ and $[\mathbf{N}_{\Gamma f}]$ are constructed from shape functions $N_{\Gamma i}$, where $i = 1, .., 4$. Given the structural similarity between the element topology used here and the 4-node Mindlin plate element presented in Section 6, we adopt the same shape functions as defined in Eq. (A.8) for $N_{\Gamma 1} = N_{s1}$, $N_{\Gamma 2} = N_{s2}$, $N_{\Gamma 3} = N_{s3}$, $N_{\Gamma 4} = N_{s4}$ inside $[\mathbf{N}_{\Gamma s}]$ and $[\mathbf{N}_{\Gamma f}]$.

Fluid-structure coupling matrix: Using the interface interpolation matrices given by Eq. (14) and Eq. (15), we establish the element fluid-structure coupling matrix $[\mathbf{r}_e]$ which results from the integration of the interface normal vector $\{\mathbf{n}_e\}$ across the interface element area Γ_e directed outside the fluid domain, hence

$$[\mathbf{r}_e] = \int_{\Gamma_e} [\mathbf{N}_{\Gamma s}]^{\mathrm{T}} \{\mathbf{n}_e\} [\mathbf{N}_{\Gamma f}] \ \mathrm{d}\Gamma \quad . \tag{16}$$

It is important to remark that the fluid-structure coupling matrix $[\mathbf{r}_e]$ is not square (12×4 in this case). It facilitates the interaction between Ω_s and Ω_f by establishing the connection between the kinematics field of Ω_s and the pressure fluctuation from Ω_f, and vice versa. Formulated for the $e-$th element of the interface Γ, this matrix can be assembled into the global system by considering the interface-solid element localisation matrix $[\mathbf{\Lambda}^e_{\Gamma s}]$ on one hand, and the interface-fluid element localisation matrix $\left[\mathbf{\Lambda}^e_{\Gamma f}\right]$ on the other:

$$[\mathbf{R}] = \sum_{e=1}^{\mathrm{NE}_\Gamma} [\mathbf{\Lambda}^e_{\Gamma s}]^{\mathrm{T}} [\mathbf{r}_e] \ \left[\mathbf{\Lambda}^e_{\Gamma f}\right] \quad . \tag{17}$$

Here, $[\mathbf{\Lambda}^e_{\Gamma s}]$ is focused on the nodes of the $e-$th element of Γ, which are shared with the Ω_s mesh. It relates the indices of the displacement degrees of freedom ($w_i, \phi_{1i}, \phi_{2i}$ with $i = 1, .., 4$) to their respective postions in the global system associated with the solid mesh. Similarly, $\left[\mathbf{\Lambda}^e_{\Gamma f}\right]$ also focuses on these shared nodes, which simultaneously belong to the Ω_f mesh. It connects the indices of their pressure degrees of freedom (p_i with $i = 1, .., 4$) to their corresponding positions in the global system associated

with the fluid mesh. In practice, both $[\mathbf{\Lambda}^e_{\Gamma s}]$ and $\left[\mathbf{\Lambda}^e_{\Gamma f}\right]$ are associated with the element assembly operation and can be implemented by attributing the element DOFs to the global system.

Implementation of the fluid-structure interactions: Based on the fluid-structure coupling matrix $[\mathbf{R}]$ as given by Eq. (17), we are ready to implement the interactions between the solid and fluid domains. This includes the pressure forces exerted on Ω_s due to the integration of p over Γ, represented by the right hand-side term of the solid domain equilibrium Eq. (12). This can be expressed as:

$$\int_\Gamma p\mathbf{n}\cdot\delta\boldsymbol{u}\ \mathrm{d}\Gamma \quad \rightarrow \quad \{\delta\mathbf{U}\}^{\mathrm{T}}[\mathbf{R}]\{\mathbf{P}\} \quad . \tag{18}$$

Similarly, we implement the continuity of accelerations imposed on Ω_f, which is represented by the right-hand side term of the fluid domain equilibrium Eq. (13). This yields:

$$-\rho_f\int_\Gamma \ddot{\boldsymbol{u}}\cdot\mathbf{n}\delta p\ \mathrm{d}\Gamma \quad \rightarrow \quad -\rho_f\{\delta\mathbf{P}\}^{\mathrm{T}}[\mathbf{R}]^{\mathrm{T}}\left\{\ddot{\mathbf{U}}\right\} \quad . \tag{19}$$

By combining Eq. (18, 19) with the expressions Eq. (A.18, B.8), we arrive at the final matrix representation of the fluid-structure interaction problem. This formulation accounts for the elastodynamics of the solid and fluid domains and their interactions through the interface.

$$\{\delta\mathbf{U}\}^{\mathrm{T}}[\mathbf{M}_s]\{\ddot{\mathbf{U}}\}+\{\delta\mathbf{U}\}^{\mathrm{T}}[\mathbf{K}_s]\{\mathbf{U}\}=\{\delta\mathbf{U}\}^{\mathrm{T}}[\mathbf{R}]\{\mathbf{P}\} \tag{20a}$$

$$\{\delta\mathbf{P}\}^{\mathrm{T}}[\mathbf{K}_f]\{\mathbf{P}\}=-\rho_f\{\delta\mathbf{P}\}^{\mathrm{T}}[\mathbf{R}]^{\mathrm{T}}\left\{\ddot{\mathbf{U}}\right\} \tag{20b}$$

Let's substitute pressure $\{\mathbf{P}\}$, which results from solving Eq. (20b), into Eq. (20a). The pressure may therefore be treated as an auxiliary variable which can be eliminated from the structural dynamic equation. This substitution leads to the condensed standard governing equation for the fluid-structure interaction problem, which can be expressed as:

$$([\mathbf{M}_s]+[\mathbf{M}_A])\{\ddot{\mathbf{U}}\}+[\mathbf{K}_s]\{\mathbf{U}\}=0 \quad . \tag{21}$$

Depending on the way the equilibrium equations governing the fluid and solid domains are solved, general FSI problems can be categorised into strong and weak coupling approaches. The former involves expressing an global equation system that includes both the fluid and solid domains, which is solved simultaneously. In comparison, the latter requires partitioned modelling of the two domains, where the governing equations are solved separately, with interpolated data transfer through the FSI interface. Therefore, this work employs a strong coupling approach, since the FSI effect acting through the interface is formulated in the form of an added mass, that is integrated into the global modal problem, which is solved once for all. The added mass matrix $[\mathbf{M}_A]$ is expressed as follows:

$$[\mathbf{M}_A]=\rho_f[\mathbf{R}][\mathbf{K}_f]^{-1}[\mathbf{R}]^{\mathrm{T}} \quad . \tag{22}$$

The added mass matrix is fully populated and obviously symmetric. It reflects the influence of the incompressible fluid on the dynamics of the structure. When the structure vibrates, it generates pressure within the fluid through its movement transmitted via the interface. As the fluid is incompressible, this

pressure is instantaneously and uniformly distributed throughout the fluid domain (with respect to the inverse of the fluid stiffness matrix). Simultaneously, the fluid exerts a pressure force on the structure in response to the acceleration of the structure imposed through the interface.

The formulation of the added mass matrix follows a standard format applicable to any discrete mechanical system that exhibits linearity and conservatism. It suggests that during free vibrations, the mechanical energy of the coupled system comprises kinetic energy from both the structure and the fluid, and potential energy only from the structural elasticity. Dynamic equilibrium is maintained as individual components of kinetic and potential energy oscillate at the frequency of vibrations, with their collective sum remaining constant. Hence, resolution of Eq. (21) yields elastodynamic solutions for the solid domain, represented by the Mindlin plate structure, with the account for the inertial effect due to the interaction with the fluid environment.

The computation of the added mass matrix can be computationally costly, particularly in cases involving complex structures tightly coupled to extensive fluid domains, such as an periodic composite plates of large sizes in contact with an ideal fluid. Therefore, in the next section, we will explore some useful simplifications within the context of infinite periodic models.

4 Periodic unit cell problem with FSI

This section aims to illustrate the construction of the FSI unit cell system that leads to a modified added mass matrix integrating the Bloch periodic boundary conditions. The unit cell enables bandgap calculations, thereby predicting vibration behaviours in periodic composite plates of large sizes. We will begin by presenting the plate and fluid domain models separately. Then, we will introduce the technique that allows coupling of the two domains with the incorporation of the periodic boundary conditions.

4.1 Plate unit cell

In this study, we assume that the composite plate exhibits translational symmetry, forming a periodic unit cell that repeats itself in four directions (including $+\boldsymbol{x}_1$, $-\boldsymbol{x}_1$, $+\boldsymbol{x}_2$, $-\boldsymbol{x}_2$) as shown in Figure 4 (a) and (b). Therefore, the dimensions of the plate unit cell are characterised by its edge lengths along the $\boldsymbol{x}_1$ and $\boldsymbol{x}_2$ axes, which are denoted as a_1 and a_2, respectively.

Currently, the periodic composite plate can be effectively represented by the plate unit cell. Due to the inherent translational symmetry in the structure, modelling the unit cell system necessitates the implementation of Bloch-Floquet boundary conditions (Bloch BCs). According to Bloch's theorem (seen Appendix C), the solution for elastic wave propagation in a periodic medium satisfies the following relation:

$$\mathbf{U}\left(\mathbf{x}+\boldsymbol{a}_i\right)=\mathbf{U}(\mathbf{x})e^{\mathrm{i}(\mathbf{k}\cdot\boldsymbol{a}_i)} \quad , \tag{23}$$

where $\mathbf{x}$ represents the position vector, and $\mathbf{k}$ is the wave vector [33]. This relationship enforces the periodicity of wave propagation solutions $\mathbf{U}$ up to a phase factor $e^{\mathrm{i}(\mathbf{k}\cdot\boldsymbol{a}_i)}$ over the extent of a unit cell $\boldsymbol{a}_i$.

We begin with the implementation of Eq. (23) on the Mindlin plate, which is isolated for illustration in Figure 4(c). It's noteworthy that the techniques used here are similar with those employed in 2D

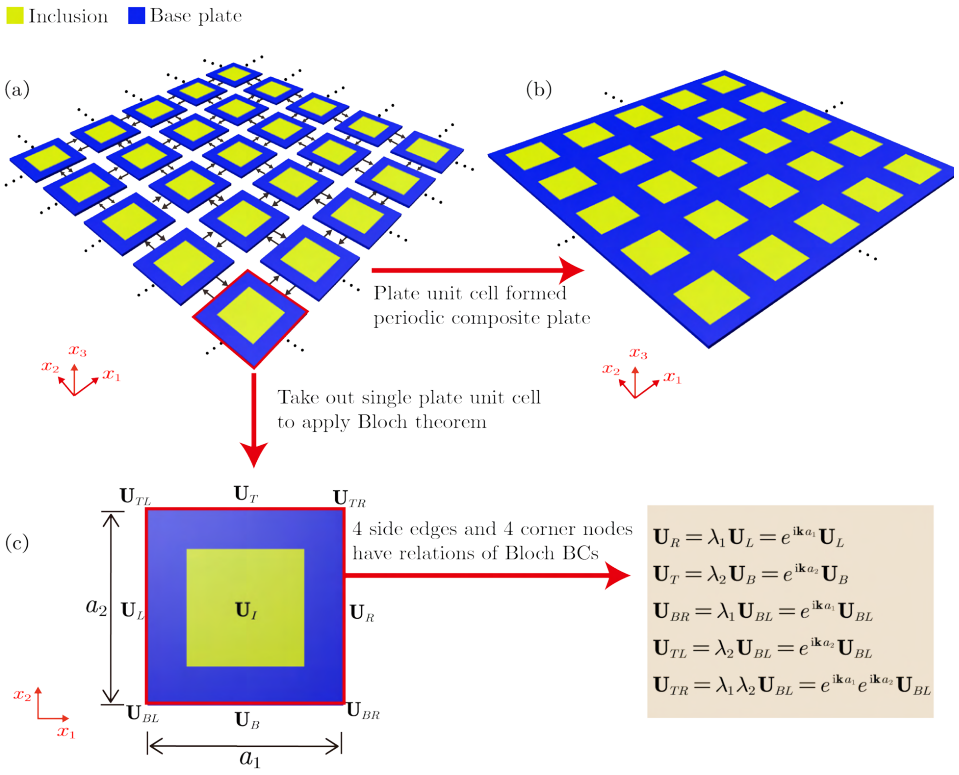

Figure 4: Periodic composite plate and its unit cell.

problems. Therefore, imposing the Bloch boundary conditions leads to constraining the Mindlin plate degrees of freedom (DOFs), which involve displacements and rotations, on opposing nodes situated on the periodic boundaries. To facilitate the notation, we categorise these DOFs into nine distinct groups as follows: $\{\mathbf{U}\} = \{\mathbf{U}_B\ \mathbf{U}_T\ \mathbf{U}_L\ \mathbf{U}_R\ \mathbf{U}_{BL}\ \mathbf{U}_{BR}\ \mathbf{U}_{TR}\ \mathbf{U}_{TL}\ \mathbf{U}_I\}^{\mathrm{T}}$. Here, the subscripts B, T, L, and R denote the DOFs of the nodes along the bottom, top, left, and right edges, respectively, excluding the four corner nodes. Subscripts BL, BR, TR, and TL correspond to the bottom-left, bottom-right, top-right, and top-left corner nodes, respectively. The remaining nodes' DOFs are indicated by the subscript I. Constraints on DOFs within these nine groups can be represented through a linear transformation denoted as $[\mathbf{T}_s]$, which is parameterised by the wave numbers $\lambda_1 = e^{\mathrm{i}\mathbf{k}\cdot\boldsymbol{a}_1}$ and $\lambda_2 = e^{\mathrm{i}\mathbf{k}\cdot\boldsymbol{a}_2}$ as follows:

$$\{\mathbf{U}\} = \begin{bmatrix} \mathbf{U}_I \\ \mathbf{U}_L \\ \mathbf{U}_R \\ \mathbf{U}_B \\ \mathbf{U}_T \\ \mathbf{U}_{BL} \\ \mathbf{U}_{BR} \\ \mathbf{U}_{TR} \\ \mathbf{U}_{TL} \end{bmatrix} = \begin{bmatrix} \mathbf{I} & 0 & 0 & 0 \\ 0 & \mathbf{I} & 0 & 0 \\ 0 & \lambda_1\mathbf{I} & 0 & 0 \\ 0 & 0 & \mathbf{I} & 0 \\ 0 & 0 & \lambda_2\mathbf{I} & 0 \\ 0 & 0 & 0 & \mathbf{I} \\ 0 & 0 & 0 & \lambda_1\mathbf{I} \\ 0 & 0 & 0 & \lambda_1\lambda_2\mathbf{I} \\ 0 & 0 & 0 & \lambda_2\mathbf{I} \end{bmatrix} \begin{bmatrix} \mathbf{U}_I \\ \mathbf{U}_L \\ \mathbf{U}_B \\ \mathbf{U}_{BL} \end{bmatrix} = [\mathbf{T}_s]\{\widetilde{\mathbf{U}}\} \quad . \tag{24}$$

4.2 Fluid unit cell

The fluid medium in contact with the periodic composite plate does not extend indefinitely in the $-\boldsymbol{x}_3$ direction. It is confined to a depth of L_3, with a rigid wall boundary employed at the bottom surface of the fluid medium, as illustrated in Figure 5 (a) and (b). The fluid under consideration is a homogeneous ideal liquid, complying with the assumptions in Section 6. The fluid domain is compartmentalised into unit cells, sharing the same periodicity as the structure domain along the $\boldsymbol{x}_1$ and $\boldsymbol{x}_2$ axes, with period lengths a_1 and a_2, respectively.

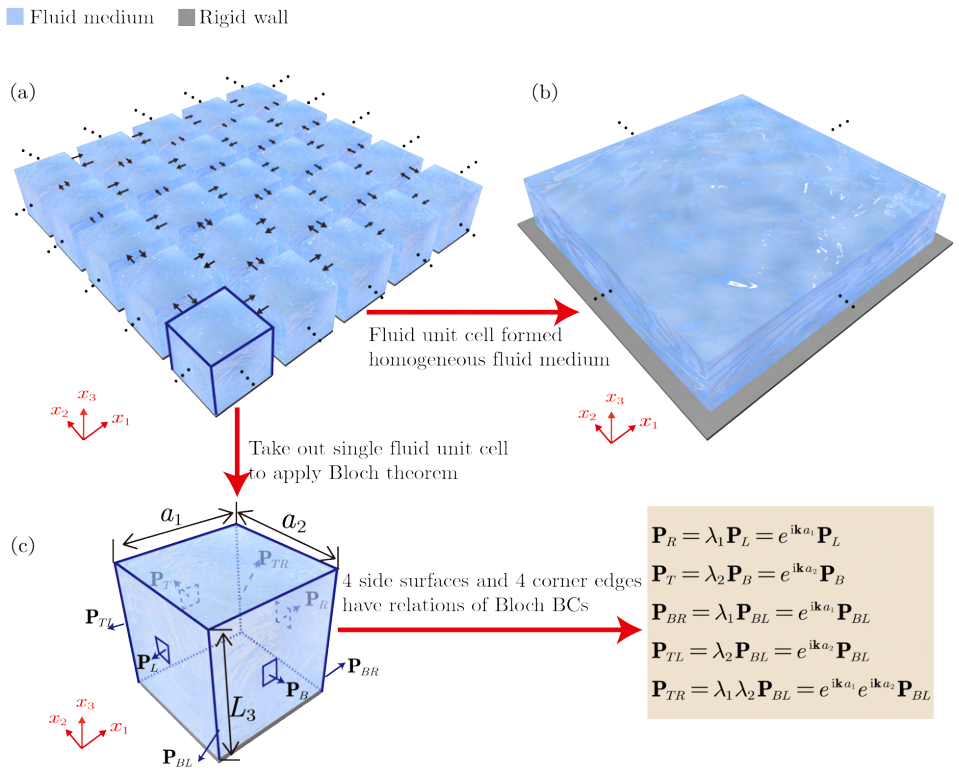

Figure 5: Fluid medium and its unit cell.

Translational periodicity of the fluid domain suggests that the field of pressure in the fluid unit cell satisfies Bloch periodic conditions on its boundaries. Therefore, the pressure field $\mathbf{P}$ exhibits periodicity across the extent of a unit cell $\boldsymbol{a}_i$ up to a phase factor $e^{\mathrm{i}(\mathbf{k}\cdot\boldsymbol{a}_i)}$:

$$\mathbf{P}\left(\mathbf{x}+\boldsymbol{a}_i\right) = \mathbf{P}(\mathbf{x})e^{\mathrm{i}(\mathbf{k}\cdot\boldsymbol{a}_i)} \quad . \tag{25}$$

This relationship (Eq. (25)), is implemented to the fluid unit cell using similar technique as employed for the plate unit cell. Subsequently, the pressure DOFs within the fluid unit cell are organised into nine categories based on the node positions, as follows: $\{\mathbf{P}\} = \{\mathbf{P}_B\ \mathbf{P}_T\ \mathbf{P}_L\ \mathbf{P}_R\ \mathbf{P}_{BL}\ \mathbf{P}_{BR}\ \mathbf{P}_{TR}\ \mathbf{P}_{TL}\ \mathbf{P}_I\}^{\mathrm{T}}$, where subscripts B, T, L, R, as well as BL, BR, TR, TL, and I carry the same interpretation as previously defined for the solid domain, but they are now associated with the respective surfaces and edges of the fluid domain. To enforce the DOF constraints within these nine groups, we use the linear transformation $[\mathbf{T}_f]$, with the wave numbers $\lambda_1 = e^{\mathrm{i}\mathbf{k}\cdot\boldsymbol{a}_1}$ and $\lambda_2 = e^{\mathrm{i}\mathbf{k}\cdot\boldsymbol{a}_2}$ as parameters. Hence, the

DOFs of the fluid domain can be expressed as:

$$\{\mathbf{P}\} = \begin{bmatrix} \mathbf{P}_I \\ \mathbf{P}_L \\ \mathbf{P}_R \\ \mathbf{P}_B \\ \mathbf{P}_T \\ \mathbf{P}_{BL} \\ \mathbf{P}_{BR} \\ \mathbf{P}_{TR} \\ \mathbf{P}_{TL} \end{bmatrix} = \begin{bmatrix} \mathbf{I} & 0 & 0 & 0 \\ 0 & \mathbf{I} & 0 & 0 \\ 0 & \lambda_1\mathbf{I} & 0 & 0 \\ 0 & 0 & \mathbf{I} & 0 \\ 0 & 0 & \lambda_2\mathbf{I} & 0 \\ 0 & 0 & 0 & \mathbf{I} \\ 0 & 0 & 0 & \lambda_1\mathbf{I} \\ 0 & 0 & 0 & \lambda_1\lambda_2\mathbf{I} \\ 0 & 0 & 0 & \lambda_2\mathbf{I} \end{bmatrix} \begin{bmatrix} \mathbf{P}_I \\ \mathbf{P}_L \\ \mathbf{P}_B \\ \mathbf{P}_{BL} \end{bmatrix} = [\mathbf{T}_f]\{\widetilde{\mathbf{P}}\} \quad . \tag{26}$$

4.3 FSI unit cell problem and its governing equation

We consider the FSI unit cell as indicated in Figure 6. Substituting the Bloch boundary conditions (Eq. (24) and Eq. (26)), into the FSI problem (Eq. (20)). We arrive at a revised governing equation:

$$\left\{\delta\widetilde{\mathbf{U}}\right\}^{\mathrm{T}}[\mathbf{T}_s]^{\mathrm{T}}[\mathbf{M}_s][\mathbf{T}_s]\left\{\ddot{\widetilde{\mathbf{U}}}\right\} + \left\{\delta\widetilde{\mathbf{U}}\right\}^{\mathrm{T}}[\mathbf{T}_s]^{\mathrm{T}}[\mathbf{K}_s][\mathbf{T}_s]\left\{\widetilde{\mathbf{U}}\right\} = \left\{\delta\widetilde{\mathbf{U}}\right\}^{\mathrm{T}}[\mathbf{T}_s]^{\mathrm{T}}[\mathbf{R}][\mathbf{T}_f]\{\mathbf{P}\}, \tag{27a}$$

$$\left\{\delta\widetilde{\mathbf{P}}\right\}^{\mathrm{T}}[\mathbf{T}_f]^{\mathrm{T}}[\mathbf{K}_f][\mathbf{T}_f]\left\{\widetilde{\mathbf{P}}\right\} = -\rho_f\left\{\delta\widetilde{\mathbf{P}}\right\}^{\mathrm{T}}[\mathbf{T}_f]^{\mathrm{T}}[\mathbf{R}]^{\mathrm{T}}[\mathbf{T}_s]\left\{\ddot{\widetilde{\mathbf{U}}}\right\}. \tag{27b}$$

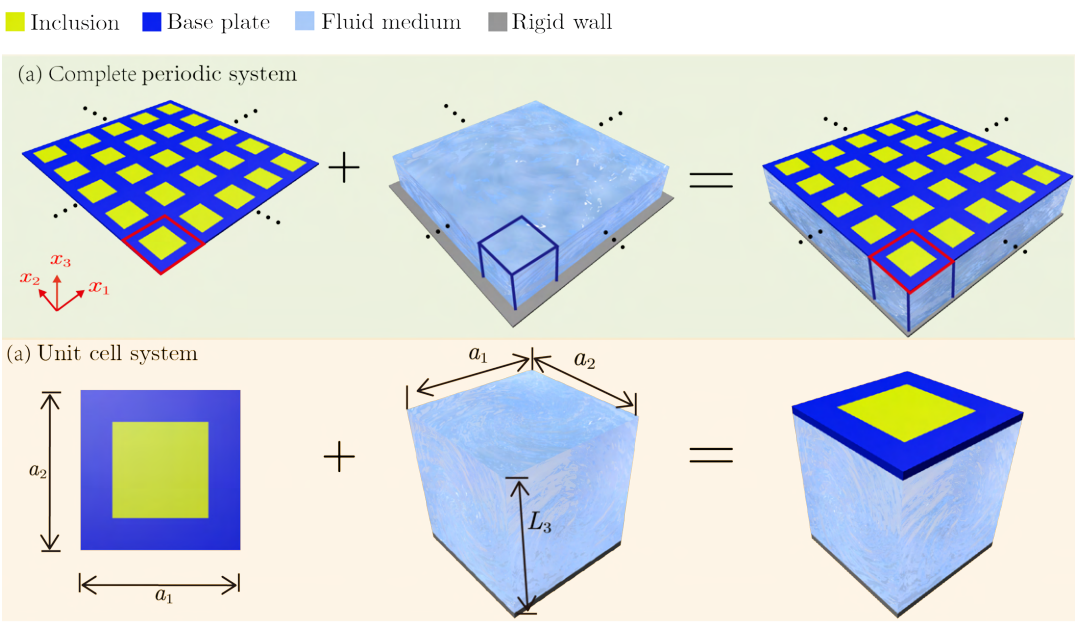

Figure 6: Periodic composite plate system and its unit cell.

Condensing Eq. (27b) and Eq. (27a) leads to the governing equation of the FSI unit cell problem:

$$\left([\mathbf{T}_s]^{\mathrm{T}}\left([\mathbf{M}_s] + [\mathbf{M}_A^{\mathrm{new}}]\right)[\mathbf{T}_s]\right)\left\{\ddot{\widetilde{\mathbf{U}}}\right\} + \left([\mathbf{T}_s]^{\mathrm{T}}[\mathbf{K}_s][\mathbf{T}_s]\right)\left\{\widetilde{\mathbf{U}}\right\} = 0 \quad . \tag{28}$$

where the new added mass matrix $[\mathbf{M}_A^{\text{new}}]$ is expressed as follows:

$$[\mathbf{M}_A^{\text{new}}] = \rho_f \, [\mathbf{R}] \, [\mathbf{T}_f] \left([\mathbf{T}_f]^{\mathrm{T}} \, [\mathbf{K}_f] \, [\mathbf{T}_f] \right)^{-1} [\mathbf{T}_f]^{\mathrm{T}} \, [\mathbf{R}]^{\mathrm{T}} \quad . \tag{29}$$

The modified added mass matrix $[\mathbf{M}_A^{\text{new}}]$ encompasses various factors, including the fluid density, the interface geometry via the fluid–structure coupling matrix, and the elastodynamics of the fluid domain represented by the fluid stiffness matrix. This new formulation facilitates the analysis of unit cell vibrations, thereby enabling predictions of vibration behaviours for periodic composite plates within the framework of fluid-structure interaction.

5 Numerical cases

This section presents three groups of numerical cases that investigate the influence of fluid-structure interaction on the vibration of periodic composite plates. First, we study the vibration bandgap based on a unit cell problem that involves a composite plate which is in contact with fluid medium, initially on one surface, then on both surfaces. Based on modal analysis, we will study the formation of the bandgaps and their evolution with the FSI properties. Particularly, we will explore the impact of FSI on anisotropic wave propagation by analyzing dispersive surfaces, phase velocities and group velocities. To evaluate the bandgap predictions, we will perform dynamic frequency analysis by calculating the frequency response functions, taking into account various unit cell geometries and full-scale plate models.

5.1 Vibration of a periodic composite plate with single side fluid structure interaction

This section investigates the impact of single-side fluid-structure interaction on the vibration behaviour of periodic composite plates. Specifically, we analyse the vibration of a bi-phase periodic composite plate with infinite repetitions along $\boldsymbol{x}_1$ and $\boldsymbol{x}_2$ directions in contact with a fluid medium on one of its surfaces, as illustrated in Figure 7 (a). As the plate does not consider the periodicity in $\boldsymbol{x}_3$ direction, we set a specific depth L_3 for the fluid medium. Therefore the fluid medium is only infinitely large along $\boldsymbol{x}_1$ and $\boldsymbol{x}_2$ directions, and the bottom surface is considered as rigid wall boundary.

To study the vibration properties, we employ a periodic cubic unit cell with dimensions of $0.2 \times 0.2 \times 0.2$ m in the $\boldsymbol{x}_1$, $\boldsymbol{x}_2$, and $\boldsymbol{x}_3$ directions. The unit cell base plate, composed of epoxy, is represented in blue in Figure 7, while the square inclusion, composed of tungsten, is represented in yellow. We chose this material combination for the base plate and inclusion to achieve broader bandgap ranges. Tungsten, with its relatively high density and stiffness compared to other metals like steel, ensures that the bandgap of the composite plate remains significant even when considering FSI. The material properties of the plate and inclusion are provided in Table 1.

The dimensions of the unit cell and its inclusion are $a_1 \times a_2 \times h = 0.2 \times 0.2 \times 0.01$ m and $c_1 \times c_2 \times h = 0.12 \times 0.12 \times 0.01$ m in the $\boldsymbol{x}_1$, $\boldsymbol{x}_2$, and $\boldsymbol{x}_3$ directions, respectively, with h denoting the plate thickness. This configuration results in an inclusion area ratio of 36% relative to the plate area. To discretise the unit cell of the fluid-structure coupled system, quadrilateral Mindlin plate finite elements are used for the solid domain and 8-node brick elements for the fluid domain. To ensure that the bandgap result remains independent of the mesh density across all frequency ranges, particularly in higher frequency

Table 1: Plate material composition

Parameters	Base plate (epoxy)	Scattering plate (tungsten)
Density ρ (kg/m^3)	1180.0	19300.0
Young's modulus E (Pa)	3.3×10^9	411.0×10^9
Poisson's ratio μ	0.33	0.28

ranges, we prescribed three distinct mesh refinements, as depicted in Figure 8.

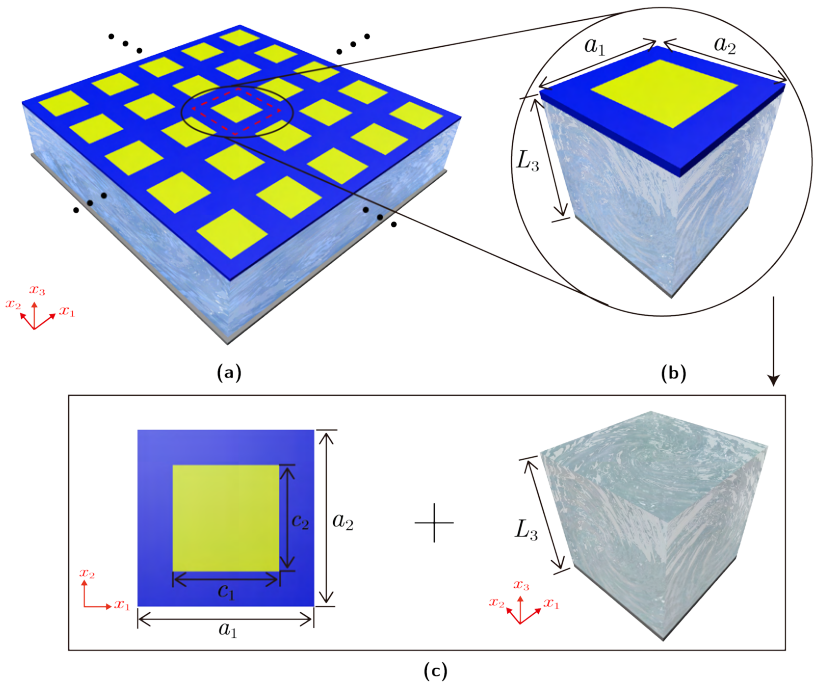

Figure 7: Example of a periodic composite plate in contact with a fluid medium by one side, and the associated unit cell: (a) whole infinite periodic model (b) whole unit cell model (c) separate unit cells in different domains.

For the vibration bandgap analysis, we compute band diagrams by considering wave vectors on the boundary of the irreducible first Brillouin zone. Due to the structural symmetry in the present study, the considered area is reduced to the edges of the triangle $\Gamma - \mathrm{X} - \mathrm{M} - \Gamma$, as shown in Figure 9. Numerically, this calculation involves sweeping the boundary path $\Gamma - \mathrm{X} - \mathrm{M} - \Gamma$ by evaluating 59 equidistant and discrete points along the path. To perform finite element analysis on the unit cell model, we apply Bloch-Floquet periodic boundary conditions to the four side boundaries associated with both the solid and fluid domains, considering wave vectors $\mathbf{k}_i = (k_{x1}, k_{x2})$ $(i = 1, 2, \ldots, \mathrm{N_{point}})$, which take different forms on each section along the path $\Gamma - \mathrm{X} - \mathrm{M} - \Gamma$. Specifically, we have: from Γ to X, $k_{x1} = \frac{\pi}{a_1}k$, $k_{x2} = 0$, $k \in [0, 1]$; from X to M, $k_{x1} = \frac{\pi}{a_1}$, $k_{x2} = \frac{\pi}{a_2}(k-1)$, $k \in [1, 2]$; then, from M to Γ: $k_{x1} = \frac{\pi}{a_1}(3-k)$, $k_{x2} = \frac{\pi}{a_2}(3-k)$, $k \in [2, 3]$. To study then potential influence of $\mathrm{N_{point}}$ on the bandgap results, we examined three distinct values of $\mathrm{N_{point}}$, which are 29, 59, and 89, as illustrated in Figure 10.

We designed six cases for this study as detailed in Table 2. Case 1 serves as the reference and only

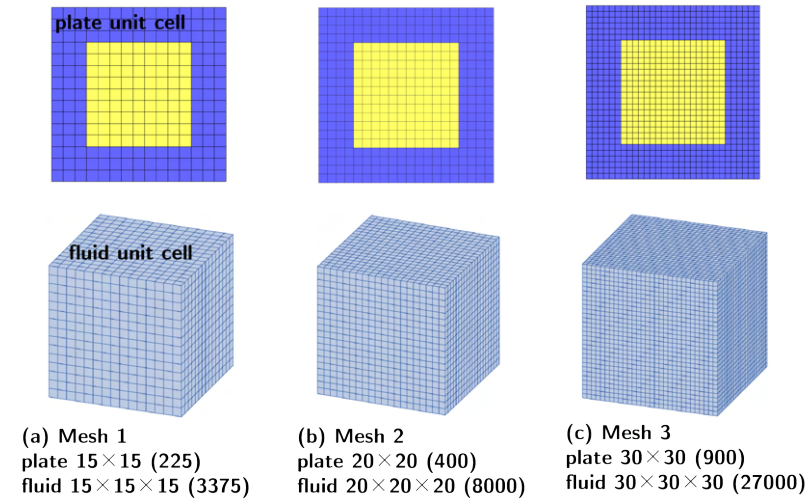

Figure 8: Different mesh configurations for the unit cell of the coupled system.

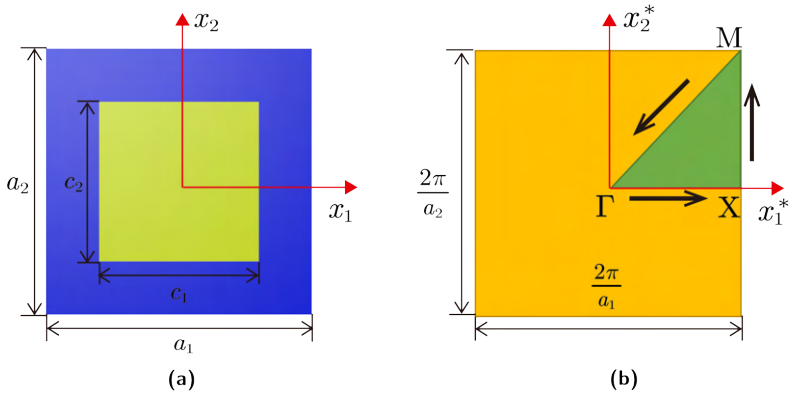

Figure 9: (a) Unit cell with rectangular inclusion (b) Representation of the irreducible first Brillouin zone on the unit cell.

considers the dry solid plate. Cases 2 through 6 involve coupling a solid plate with a fluid medium on one side of the plate. In particular, Cases 2 to 4 prescribe three different liquid densities, which correspond to water, pentane, and iodomethane, while Cases 5 and 6 feature varying depths of the fluid L_3.

We start by conducting analysis to ensure the independance of the bandgap results with respect to mesh refinement and the value of $\mathrm{N_{point}}$, using Case 1 and Case 2. From Figure 11, the band structures have converged, even for the highest-order band curve that represents the highest frequencies considered in the study, with the mesh density surpassing that of Mesh 1. In particular, Case 2 exhibits better convergence, as the consideration of FSI has reduced the frequency range of high-order band curves. Figure 12 shows that $\mathrm{N_{point}}$ has a minor influence on the convergence of the band structure, although it leads to linearly increased computation time. In essence, $\mathrm{N_{point}}$ primarily affects the smoothness of the band curves. Therefore, we opt to use Mesh 2 and $\mathrm{N_{point}} = 59$ for all cases in this section, as it represents a balance between computational cost and convergence of band structures especially in the high-frequency range.

Then, with the parameters defined above, the band diagrams calculated based on the unit cell of

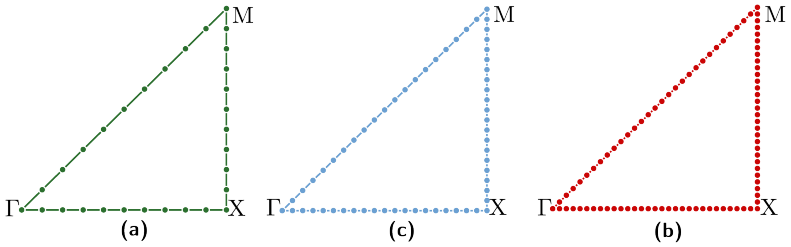

Figure 10: Discrete points on K-path with different N_{point}: (a) N_{point}=29 (a) N_{point}=59 (a) N_{point}=89.

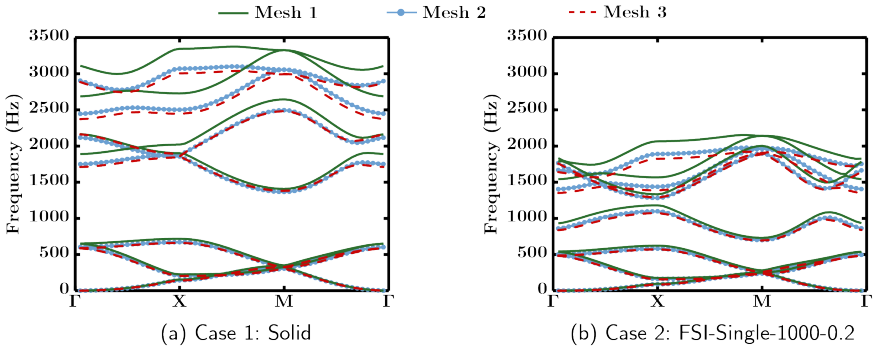

Figure 11: Bandgap diagram of Case 1 and Case 2 with different mesh densities.

the plate with fluid on one side are depicted in Figure 13. Figure 14 displays the vibration mode shapes associated with the 4th branch of the band structure at point A, highlighted with red circles in Figure 13. Figure 15 presents the iso-frequency contours, which serve as the basis for phase velocities analysis and group velocities analysis, presented from Figure 16 to Figure 17.

Bandgap analysis and the associated mode shapes:

Bandgaps usually emerge from the interactions among periodically repeating units within the structure. It refers to the phenomenon where specific frequencies of waves encounter impediments or undergo attenuation within its designated frequency range, particularly within the bandgap region. For instance, in Case 1, when an external force is applied exclusively at 1000Hz (falling within the bandgap region) to a periodic composite plate, the induced structural response will be significantly diminished compared

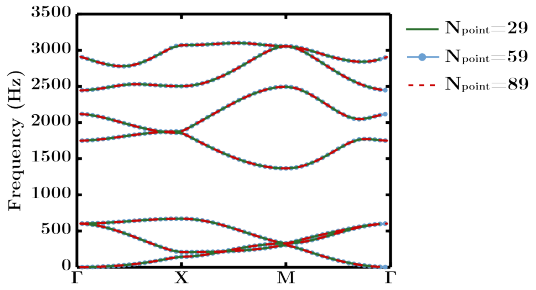

Figure 12: Bandgap diagram of Case 1 with different N_{point}.

Table 2: Case configurations

Case index	Model	ρ_f (kg/m^3)	L_3 (m)
1	Solid only	/	/
2	Single-side FSI	1000.0	0.2
3	Single-side FSI	626.0 (pentane)	0.2
4	Single-side FSI	2280.0 (iodomethane)	0.2
5	Single-side FSI	1000.0	0.1
6	Single-side FSI	1000.0	0.4

to the scenario where the external force is applied solely at 500Hz (outside the bandgap region).

A comparison between Case 2 and Case 1, as depicted in Figure 13 (a) and (b), highlights the impact of the fluid environment on the structure's vibration due to the coupling between fluid inertia and the structure. The added mass effect induces a general reduction in the natural frequency responses, which is particularly noticeable at higher natural frequencies, where frequency levels exhibit a substantial decrease due to fluid-structure interaction. This added mass effect on higher natural frequencies results in remarkable changes in the structure's vibration bandgaps. Consequently, the first bandgap of Case 1 undergoes a significant reduction in bandwidth, contracting from 694 Hz (range $[670.8 - 1365.4]$ Hz) to 118 Hz (range $[581.5 - 699.7]$ Hz). This contraction can be attributed to the significant decrease in the frequency level of the 4th band curve. Furthermore, this modification gives rise to a new narrow bandgap within the range of $[1097.4 - 1282.0]$ Hz, which is not present in Case 1. In Cases 2 to 4, as depicted in Figure 13 (b) to (d), an increase in fluid density is observed to lower the natural frequencies, subsequently reducing the bandwidth of the vibration bandgaps. Therefore in Case 3 (fluid density of 626.0 kg/m^3), two full bandgaps emerge within the ranges $[610.6 - 817.5]$ Hz and $[1239.6 - 1437.6]$ Hz, formed by the 3rd and 4th, and the 4th and 5th band curves, respectively. Then in Case 4, only one full bandgap is observed, spanning the range $[834.3 - 976.3]$ Hz, created by the 4th and 5th band curves.

Despite these changes, the fluid environment does not induce significant effect on the vibration mode shapes. As illustrated in Figures 14 (a) and (b), the mode shape remains predominantly unchanged, despite the considerable decrease in natural frequencies observed in Case 2 compared to Case 1 (without fluid environment), due to the account for fluid-structure interaction. Similarly, variations in fluid density only result in limited impact on the vibration mode shape, which can be confirmed by comparing Figures 14 (b) to (d). Hence, the effect of homogeneously distributed added mass on the composite plate significantly affects its vibration responses by lowering its natural frequencies. The vibration bandgaps evolve as if the composite plate behaves with additional mass, but the effect of added mass exhibits limited influence on the vibration mode shape.

We subsequently study the influence of the fluid domain depths. Therefore, we prescribe in Cases 2, 5, and 6 three fluid domain depths (L_3) of 0.2 m, 0.1 m, and 0.4 m, respectively, as depicted in Figure 13 (b), (e), and (f). The two full bandgaps in Case 5 ($L_3 = 0.1$ m) span the ranges $[581.4 - 694.0]$ Hz and $[1094.7 - 1281.4]$ Hz. For Case 6 ($L_3 = 0.4$ m), the two full bandgaps cover the ranges $[581.5 - 699.7]$ Hz and $[1097.5 - 1282.0]$ Hz. It becomes evident that the bandgaps in these three cases remain nearly constant as the fluid domain depth (L_3) increases from 0.2 m to 0.4 m. This observation suggests that once the fluid volume is sufficiently large, its impact on the bandgaps and natural frequencies of the solid becomes insignificant. The consistent mode shapes across the three cases, as shown in Figures 14 (b), (e), and (f), further confirm this conclusion. We therefore neglect the factor of the fluid domain

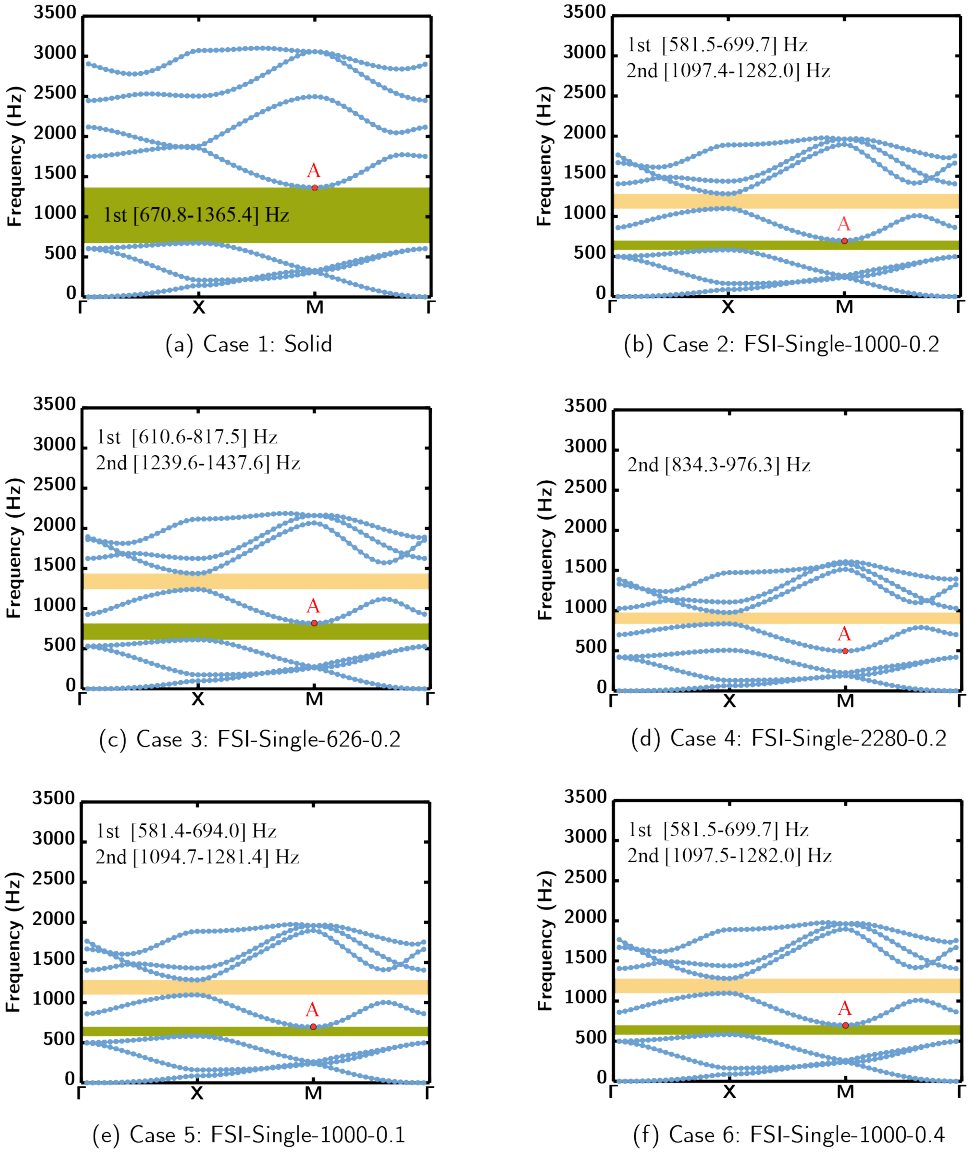

Figure 13: Bandgap diagrams of cases with single side fluid.

depth for consideration in subsequent investigations.

Dispersive surface, phase velocities and group velocities:

The iso-frequency contour, also referred to as the dispersive surface, is calculated across the entire first Brillouin zone. By sweeping the wave vector $\mathbf{k}$ over all points within and on the boundary of the first Brillouin zone, we derive the complete eigenfrequency surface $\omega = \omega(\mathbf{k})$ corresponding to various dispersion branches. The dispersion surfaces illustrate the frequency distribution for each order of eigenfrequencies and represent an important tool for studying the anisotropy of wave propagation.

Here, we focus on the 1st mode, as well as the 3rd, 4th, and 5th order modes in the vicinity of the bandgaps, as depicted in Figure 15. We observe that the wave propagation within the periodic composite structure exhibits significant anisotropy across a wide frequency spectrum, with the iso-frequency contours changing more rapidly along the clinodiagonal direction compared to the horizontal and vertical directions. Notably, the 1st mode demonstrates weaker anisotropy compared to the higher

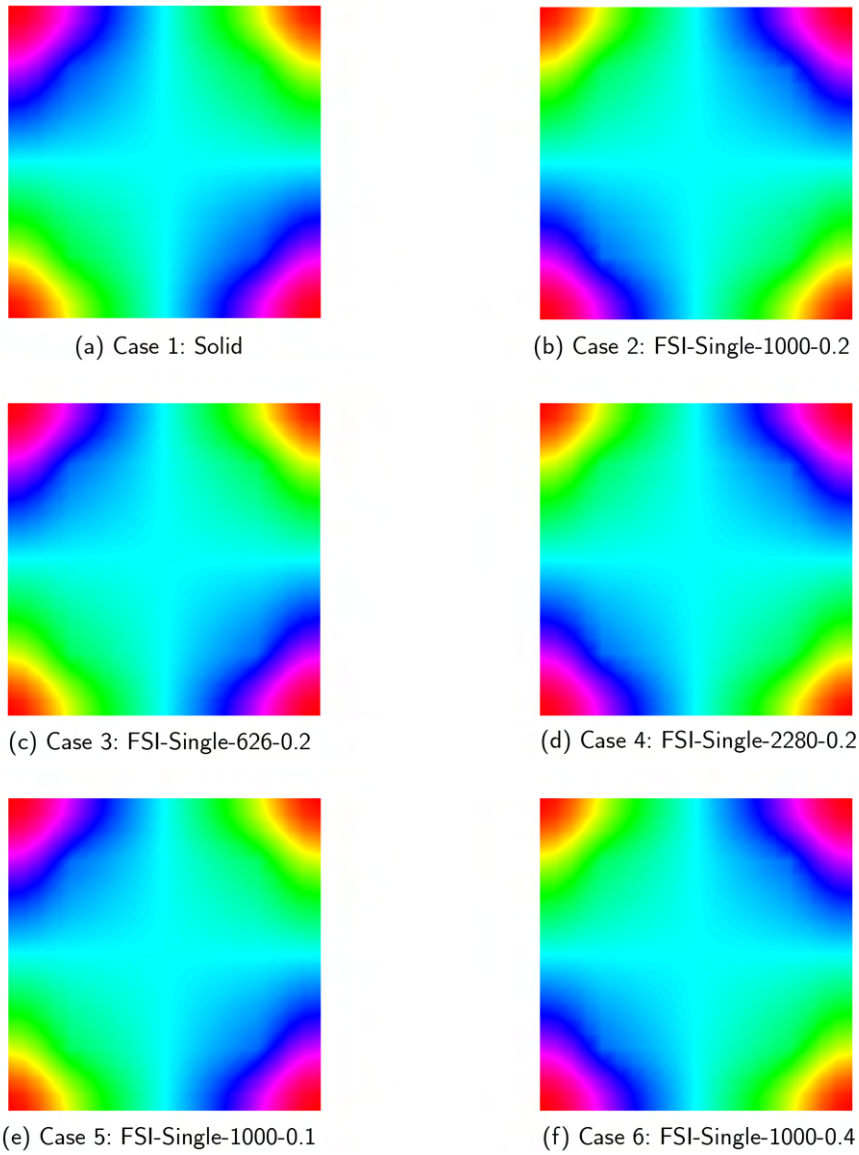

(a) Case 1: Solid (b) Case 2: FSI-Single-1000-0.2

(c) Case 3: FSI-Single-626-0.2 (d) Case 4: FSI-Single-2280-0.2

(e) Case 5: FSI-Single-1000-0.1 (f) Case 6: FSI-Single-1000-0.4

Figure 14: Mode shape of cases with single side fluid.

order modes. Meanwhile, the influence of fluid added mass is more pronounced on the 4th and 5th modes than on the lower order 1st and 3rd modes. These effects are particularly concentrated near the center of the contours. The low-frequency portion of the wave, when considering FSI, tends to exhibit characteristics of full 360° propagation, which is especially remarkable in the 5th mode.

Analysis of phase velocities and group velocities provides further insight into the anisotropic wave propagation and the associated energy flow in periodic structures. The phase velocity ($\mathrm{V_{ph}}$) of two-dimensional periodic structures for a given frequency can be expressed as $\mathrm{V_{ph}} = \frac{\omega}{\mathbf{k}}$, where $\mathbf{k} = (k_{x1}, k_{x2})$. Similarly, the group velocities along the $\boldsymbol{x}_1$ and $\boldsymbol{x}_2$ directions for a given frequency are expressed as $\mathrm{V_{gx1}} = \frac{\partial \omega}{\partial k_{x1}}$ and $\mathrm{V_{gx2}} = \frac{\partial \omega}{\partial k_{x2}}$, which are defined as the gradient of an iso-frequency curve. The direction of the outer normal at each point on the iso-frequency contour aligns with the group velocity direction, indicating the energy propagation direction of the vibration at that frequency. Therefore, by calculating the gradient at each point on the iso-frequency contour, we can determine both the

propagation direction and the corresponding region of propagation for a given vibration frequency.

As depicted in Figures 16 and 17, we illustrate phase velocity and group velocities corresponding to different frequencies. For the 1st and 3rd modes, we fix the frequency values at 100Hz and 450Hz, respectively. For the 4th mode, we select relatively high frequencies within each iso-frequency contour, while for the 5th mode, we opt for relatively low frequencies within each contour. The discrepancies between phase velocity and group velocity across all cases, with and without the fluid added mass effect, exhibit pronounced dispersive behaviour. In Figure 17 (a)-(d), the distributions of group velocity in the 1st mode at 100 Hz indicate that the presence of the fluid medium leads to a concentration of energy flow from all directions (Case 1) towards the diagonal directions (Cases 2-4), where clusters of velocities significantly increase with higher fluid density. This demonstrates a pronounced energy aggregation along the k_{x1} and k_{x2} directions, suggesting weaker energy propagation in these directions compared to the diagonal direction, as indicated by the smaller clusters of group velocities. On the contrary, for the 5th mode, increasing fluid density tends to broaden the energy flow direction of low-frequency waves from the k_{x1} and k_{x2} directions to all directions.

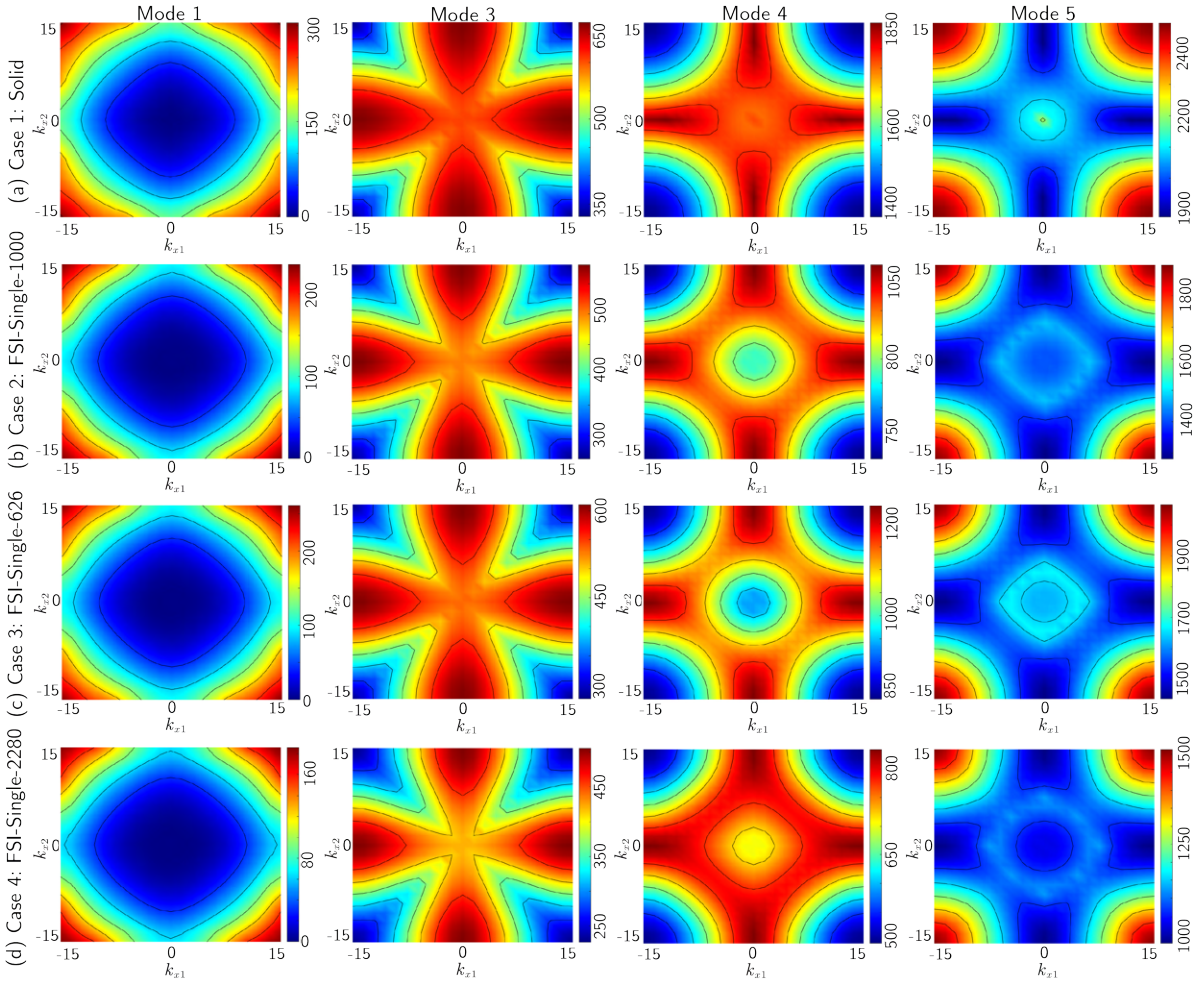

Figure 15: Iso-frequency contours of cases with single side fluid.

In conclusion, the results of this study reveal that for periodic composite plates with single-side fluid-structure interaction, the introduction of fluids results in homogeneously distributed added mass, leading to a reduction in the plate's natural frequencies and subsequent modifications in its vibration bandgaps.

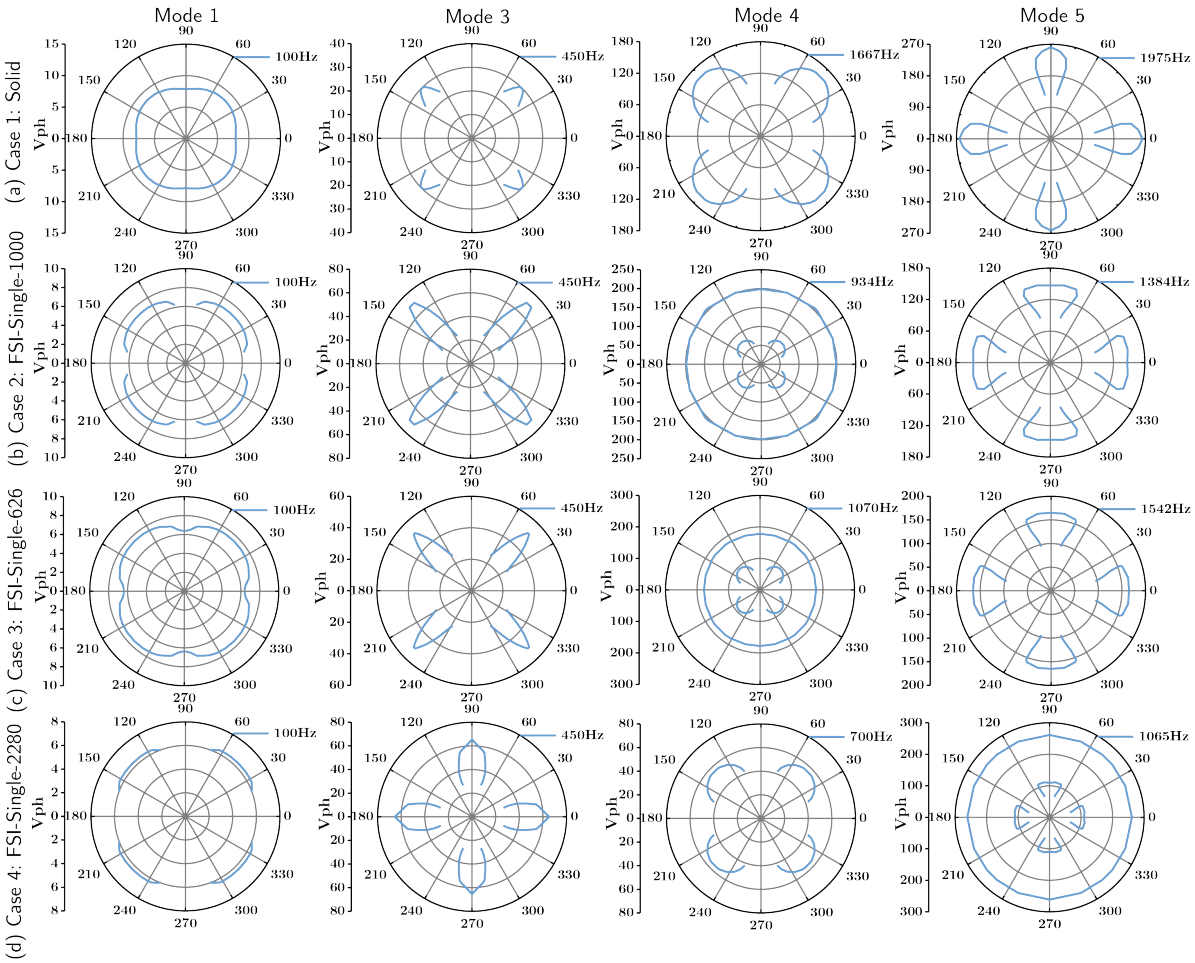

Figure 16: Phase velocities of cases with single side fluid.

This influence is amplified with increased fluid density, while the depth of the fluid environment exerts only a limited effect. In addition, the presence of the fluid does not significantly alter the plate's mode shape, indicating the pure inertial effect of fluids that act upon the plate structure. Furthermore, the existence of fluid medium will also influence the vibration behaviour of the periodic structure outside the bandgap range, especially on the wave propagating directions on some specific frequencies.

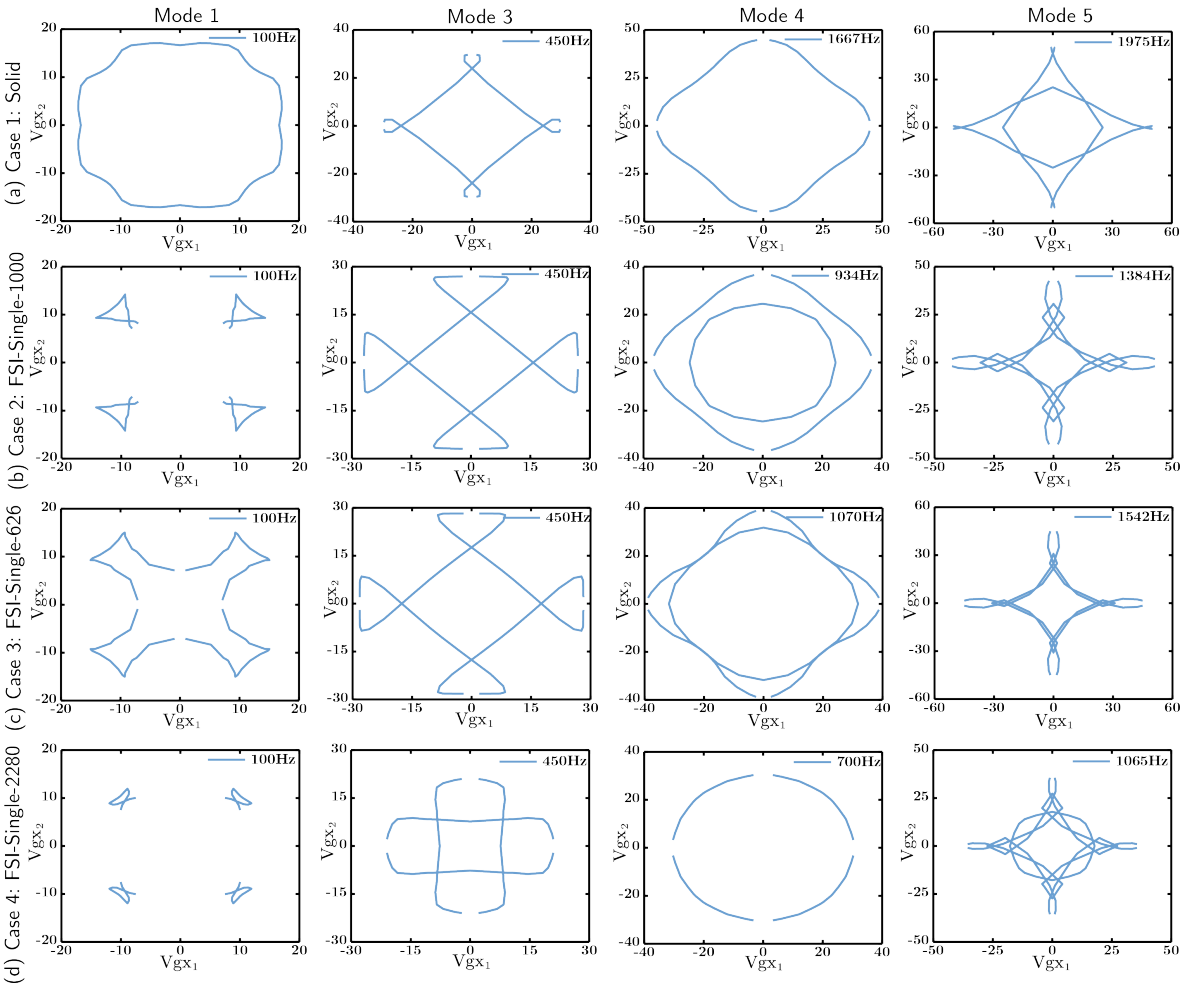

Figure 17: Group velocities of cases with single side fluid.

5.2 Vibration of a periodic composite plate with double-side fluid structure interaction

In practical situations, a plate might be in contact with fluids on both sides instead of just one. Consequently, this section investigates a double fluid cavity configuration involving a vibrating composite plate with double-sided fluid-structure interaction. Consequently, this section investigates a double fluid medium configuration involving a vibrating periodic composite plate with double-sided fluid-structure interaction.

This investigation aims to study the effect of added mass due to fluid inertia from both sides of the plate. As depicted in Figure 18 (a), the periodic composite plate is in contact with fluid mediums (ideal incompressible, non-viscous fluids) on both sides. The fluid mediums have infinite dimensions along $\boldsymbol{x}_1$ and $\boldsymbol{x}_2$ directions, similar to the periodic composite plate, but are bounded by a limited depth L_3 in the $\boldsymbol{x}_3$ direction. The remaining surfaces of the fluid mediums, including one top surface and one bottom surface, are considered as rigid wall boundaries. The vibration behaviour of the system is studied based on a periodic unit cell, as shown in Figure 18 (b). The unit cell comprises a solid domain representing the unit plate microstructure, which is in contact with a fluid domain on both sides. The side surfaces of the unit cell, including those of the fluid domain and the four edges of

the unit plate, incorporate Bloch-Floquet boundary conditions to represent the unit cell as part of a continuous periodic domain. The fluid unit cells are bounded by rigid walls on the top and bottom surfaces. The unit cell dimensions are $a_1 \times a_2 \times h = 0.2 \times 0.2 \times 0.01$ m in the $\boldsymbol{x}_1$, $\boldsymbol{x}_2$, and $\boldsymbol{x}_3$ directions for the solid domain and $a_1 \times a_2 \times L_3 = 0.2 \times 0.2 \times 0.2$ m in the $\boldsymbol{x}_1$, $\boldsymbol{x}_2$, and $\boldsymbol{x}_3$ directions for the fluid unit cells. The material parameters for the solid and wave vector settings are consistent with those described in Section 5.1.

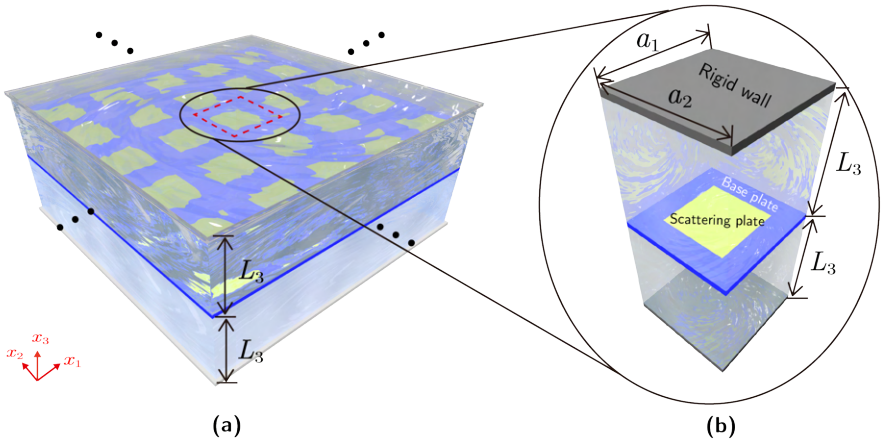

Figure 18: Example of a periodic composite plate in contact with double-side fluid mediums (a), and the periodic unit cell (b) subject to bandgap calculations.

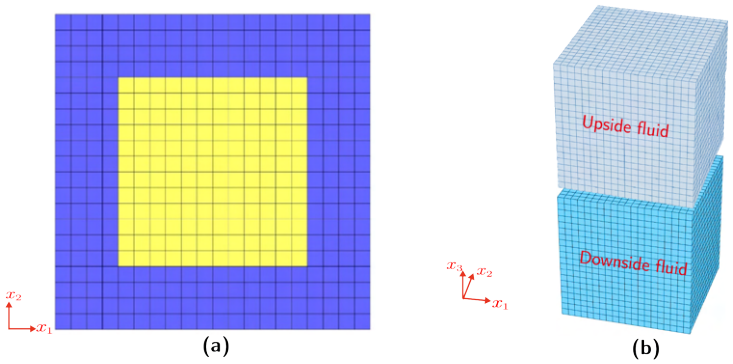

Figure 19: Mesh of the unite cell of the coupled system: (a) Using 20×20 mesh with rectangular elements to divide the solid cell (b) Using $20 \times 20 \times 20$ mesh with cubic elements to divide the fluid cell.

The unit cell of the coupled system is discretised using quadrilateral plate elements, as detailed in Section 6 for the solid domain (Figure 19 (a)), and 8-node hexahedral elements for the fluid domain (Figure 19 (b)). Concerning the mesh density, the element edge length is set to 0.01 m. Despite the symmetric nature of the unit cell structure, the top and bottom fluid domains are meshed independently.

We consider in this study three cases, as outlined in Table 3. For each case, the lower fluid domain is filled with one of three distinct fluids with varying densities, while water is consistently used as the fluid for the upper cavity. Considering the linear material behaviours, it is expected that the superposition principle can be applied to predict the plate vibration behaviour by combining the effects of different

Table 3: Case configurations

Case index	Model	$\rho_{(\text{upper})}$ (kg/m^3)	$\rho_{(\text{lower})}$ (kg/m^3)	L_3 (m)
7	Double-side FSI	1000.0	1000.0	0.2
8	Double-side FSI	1000.0	626.0	0.2
9	Double-side FSI	1000.0	2280.0	0.2

fluid densities. As previously stated in Section 5.1, the depths of the fluid domains remain constant at $L_3 = 0.2$ m.

Bandgap analysis and the associated mode shapes:

The vibration band diagrams associated with the composite plate featuring double-sided fluid-structure interaction are depicted in Figure 20. A comparison of Case 7 and Case 2, as shown in Figure 13 (b) and Figure 20 (a), reveals that accounting for fluid-structure interaction on both sides of the composite plate results in a greater reduction in natural frequencies compared to cases involving water on only one side of the plate. This frequency reduction is especially pronounced at higher natural frequencies. Consequently, the bandgaps $[581.5 - 699.7]$ Hz and $[1097.4 - 1282.0]$ Hz, observed in Case 2 with single-sided fluid-structure interaction and a single water cavity, narrow down to $[520.1 - 529.8]$ Hz and $[876.2 - 1025.4]$ Hz in Case 7, which involves double-sided water mediums. The first bandgap, in particular, experiences a significant reduction, with its bandwidth contracting to a mere 8.7 Hz. Figure 21 further illustrates the mode shapes in terms of vibration amplitude, corresponding to the 4th band curve at point A, as highlighted by red circles in Figure 20. A comparison of Figure 14 (b) and Figure 21 (a) indicates no substantial changes in the vibration mode shapes between Cases 2 and 7. This observation suggests that the presence of water on both sides of the plate results in a superposition effect of the added mass, leading to further reduced natural frequencies and bandgap widths without impacting the associated mode shapes.

In Cases 7 to 9, as illustrated in Figures 20 (a) to (c), we examine the influence of varying fluid densities in the lower cavity while maintaining water in the upper cavity. This allows us to observe the consequent changes in bandgap behaviour. The results indicate that an increase in fluid density augments fluid inertia, thereby enhancing the added mass effect on the vibration behaviour. This leads to a reduction in both natural frequency levels and bandgap ranges. Consequently, the first bandgap $[540.6 - 572.7]$ Hz observed in Case 8 with $\rho_{(\text{lower})} = 626.0$ kg/m^3 disappears when the fluid density increases to $\rho_{(\text{lower})} = 2280.0$ kg/m^3 (Case 9), and the second bandgap $[940.3 - 1102.3]$ Hz narrows down to $[725.1 - 846.1]$ Hz. Regarding the vibration mode shapes, as depicted in Figures 21 (a) to (c), altering the fluid density on one side of the plate does not affect the associated mode shapes. This observation suggests that the impact of the added mass remains constant, irrespective of whether fluid inertia is applied from one or both sides of the plate.

Dispersive surface, phase velocities and group velocities:

Figure 22 presents the iso-frequency contours of cases with fluid on both sides, displaying the 1st, 3rd, 4th, and 5th order modes, as shown in Figure 22. These contours exhibit the characteristic of changing rapidly in the clinodiagonal direction while becoming flatter in the horizontal and vertical directions, akin to Figure 15. This suggests that the anisotropic behaviours of the composite plate are solely associated with the solid structure and are not influenced by the number of sides in contact with the fluid medium. Significant changes are observed in the center of the contour, where the value tends

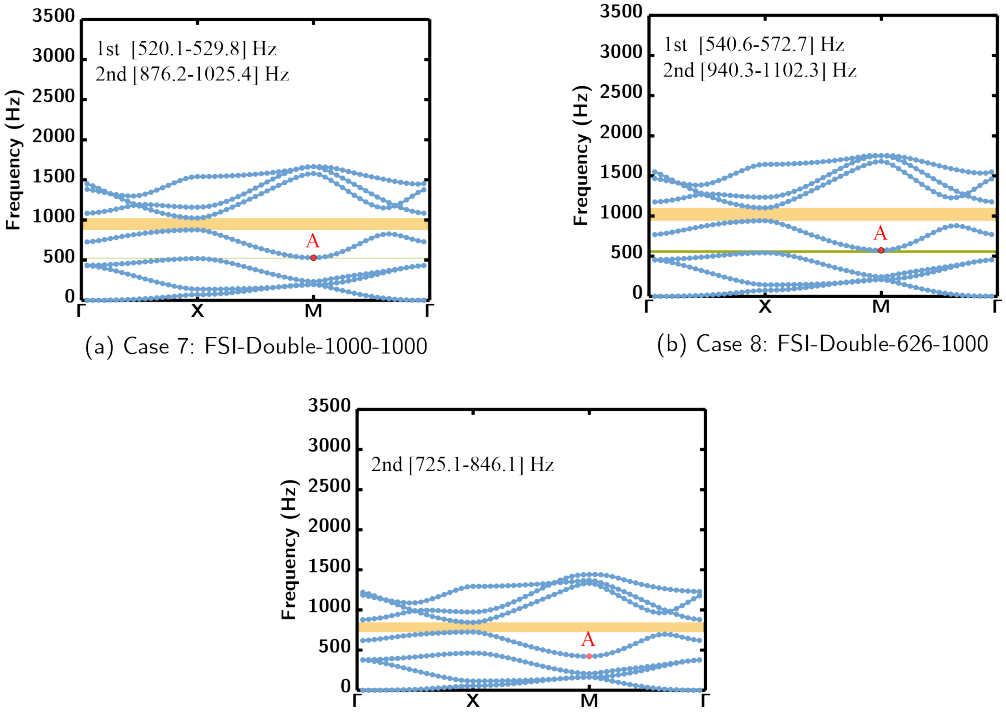

Figure 20: Bandgap diagrams of cases with two sides fluid.

to shift to a higher frequency in the 4th mode with an increase in fluid density, and conversely, the value shifts to a lower frequency in the 5th mode. Except for the 1st mode, the maximum and minimum frequency values are located at the corner points and the midpoints of the edges, corresponding to the X and M points on the band diagram path $\Gamma - X - M - \Gamma$ and forming the bandgap regions.

Based on the iso-frequency contour in Figure 22, the phase and group velocities are plotted in Figure 23 to Figure 24. Similar to Section 5.1, different frequency values are chosen for each mode. The differences between phase velocity and group velocity for cases with fluid on both sides illustrate strong dispersive behaviour in these cases. In Figure 24 (a)-(d), the group velocities in the 1st mode all concentrate on the diagonal directions. Simultaneously, with an increase in the density of the fluid on the lower side, the degree of concentration is further enhanced, and the magnitude of group velocity at $100, \mathrm{Hz}$ in the 1st mode decreases. Regarding the distribution of group velocities of the 3rd mode with a constant frequency value of $450, \mathrm{Hz}$, the shapes change from concave to convex with an increase in the density of the fluid on the lower side, indicating a weakening of directional concentration of energy flow. A similar situation is also observed in the group velocities of the 5th mode.

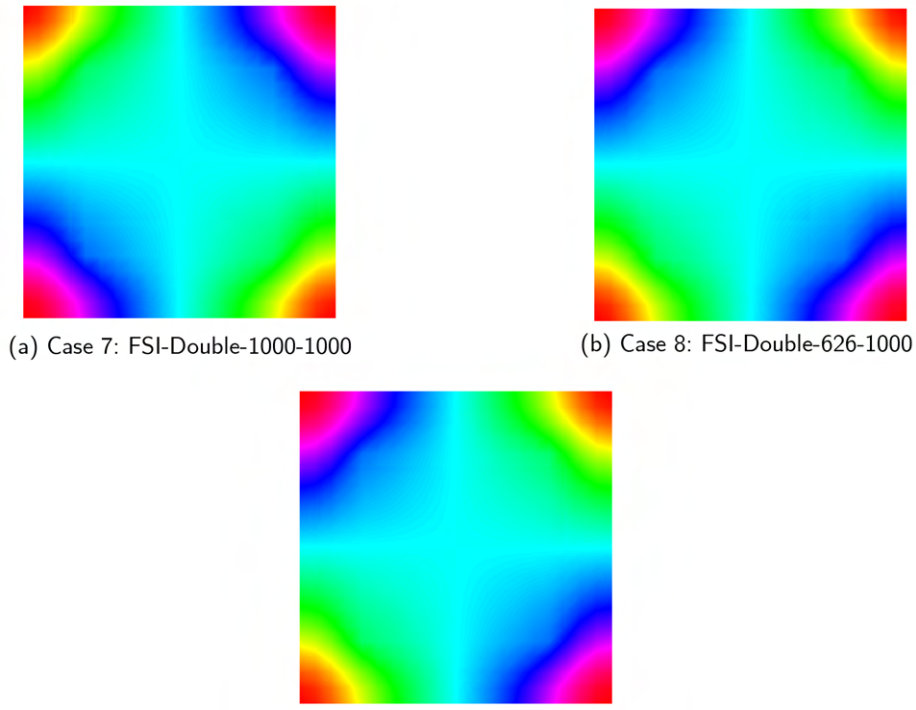

(a) Case 7: FSI-Double-1000-1000

(b) Case 8: FSI-Double-626-1000

(c) Case 9: FSI-Double-2280-1000

Figure 21: Mode shapes of cases with two sides fluid.

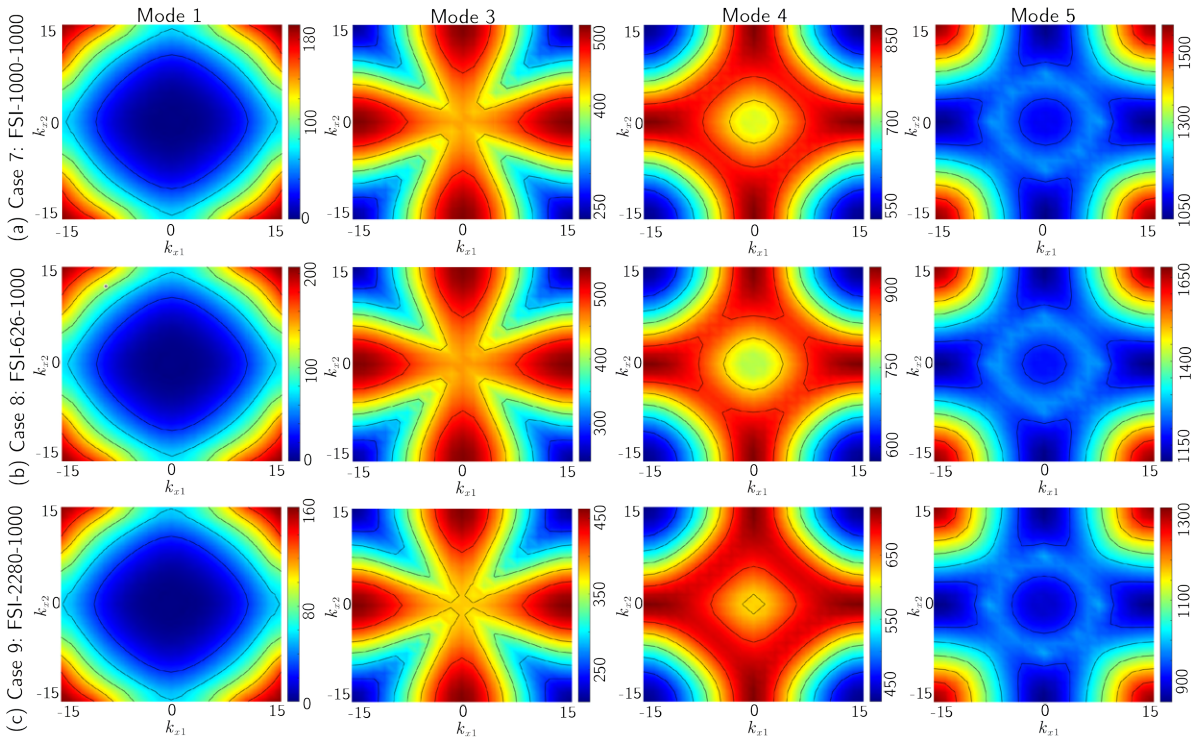

Figure 22: Iso-frequency contours of cases with two sides fluid.

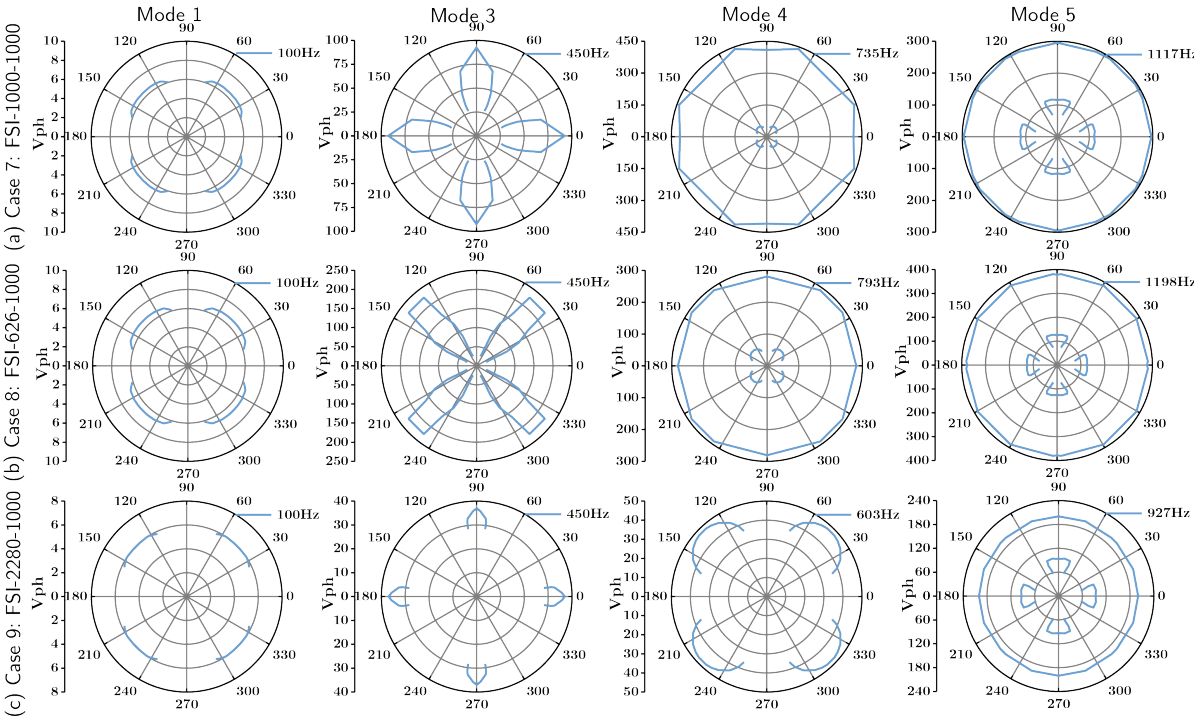

Figure 23: Phase velocities of cases with two sides fluid.

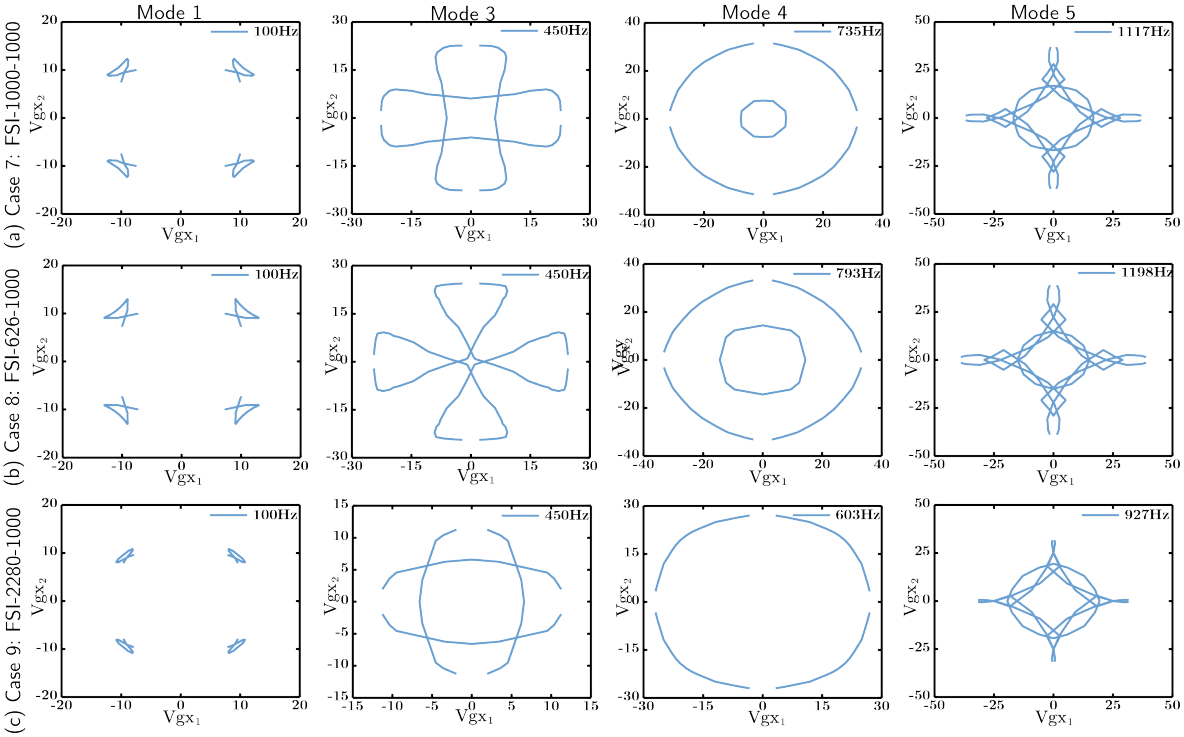

Figure 24: Group velocities of cases with two sides fluid.

5.3 Dynamic response analysis

In the preceding section, bandgap predictions were conducted for the unit cell within infinitely extended periodic structures. However, it is important to acknowledge the practical challenges associated with manufacturing a periodic composite plate featuring an infinite repetition of unit cells in both the $\boldsymbol{x}_1$ and $\boldsymbol{x}_2$ directions. For the experimental tests carried out in the laboratory, such plates are often constrained by finite dimensions. Therefore, in this section, we extend our investigation to the experiments which may be done in the future with finite periodic composite plate considering fluid inertial effects. We accomplish this by performing dynamic response analyses in the frequency domain, taking into consideration the limitations imposed by the finite size of the structure.

These analyses focus on representative structures consisting of periodic unit cells with different types of solid boundary conditions, and the results will be compared to bandgap predictions, considering both the presence and absence of fluid inertial effects. It should be clarified that these different solid boundaries will only be applied to the dynamic response analysis of the full-scale structure and are unrelated to the bandgap analysis of a single unit cell. Moreover, this section aims to showcase the versatility of the developed method when applied to periodic composite plates that incorporate intricate geometrical configurations.

The frequency domain dynamic response is obtained using the frequency response function (FRF) as detailed in Appendix D, which calculates the steady-state dynamic response of a complete full-scale structure concerning sinusoidal input excitation adopting the transfer function $[\mathbf{H}]$ in Eq. (D.11).

We present two examples of full-scale periodic composite plates with single-side fluid-structure interaction for analysis. These composite plates consist of 25 unit cells arranged along the $\boldsymbol{x}_1$ and $\boldsymbol{x}_2$ directions, featuring square and octagonal star inclusions, as depicted in Figure 25. The plate's dimensions are $L_1 \times L_2 = 1 \times 1$ m in the $\boldsymbol{x}_1$ and $\boldsymbol{x}_2$ directions, with a thickness of 0.01 m. In both cases, one side of the composite plate is submerged in a fluid cavity with a depth L_3 of 0.2 m. For the octagonal star inclusion, we use $2b$ to represent its outer diameter and $2c$ for the inner diameter, with $2b = 0.18$ m and $2c = 0.10$ m. The plate material parameters and mesh density for the various material domains remain consistent with those described in Section 5.1.

In the 25-cell fluid-structure system, the plate and fluid domains no longer extend indefinitely in the x_1x_2 plane but have finite size ranges. Therefore, the periodic boundaries will not be used for the four side boundaries of the plate and fluid anymore. Instead, we consider the fluid medium to be contained in a fluid cavity, in which the four side surfaces are defined as rigid walls, with the exception of the top surface in contact with the 25-cell composite plate. Regarding the plate, three different kinds of boundary conditions are considered: all four side edges are clamped, simply supported, or free, as shown in Figure 26. An input excitation $\mathcal{F}_3 = \mathcal{F}e^{\mathrm{i}\omega t}$ is applied at the point $(x_1, x_2) = (0.5, 0.5)$ m. As the input wave signal propagates through the plate structure, the steady-state dynamic response is recorded at the point $(x_1, x_2) = (0.1, 0.5)$ m, as illustrated in Figure 25. By analyzing the output dynamic response with respect to the input excitation, we can draw comparisons with the bandgap predictions.

Figures 27 and 28, (a) and (e), (b) and (f), (c) and (g), illustrate the frequency responses of the composite plate with square and octagonal inclusions adopting different boundary conditions, both with and without accounting for the effect of fluid-structure interaction, calculated using frequency response functions (FRFs). The vibration bandgap predictions based on the respective unit cell calculations are provided in Figures 27 and 28 (d) and (h) for comparison. Remarkably, the predicted bandgap

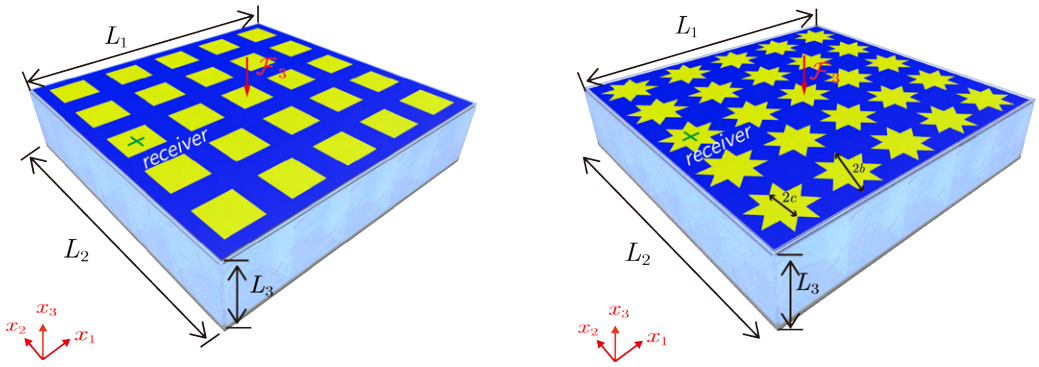

(a) Inclusion with rectangular shape (b) Inclusion with rectangular shape

Figure 25: A twenty-five-cell system of periodic composite plate with ideal fluid cavity used for dynamic response analysis in frequency domain: red arrow indicates input excitation; green cross refers to the position of output wave measurement.

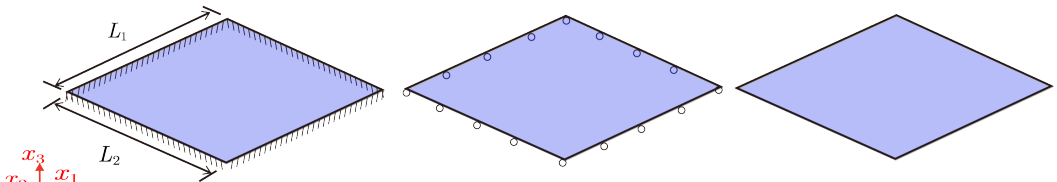

(a) Plate with all clamped boundarys (CCCC) (b) Plate with all simply supported boundarys (SSSS) (c) Plate with all free boundarys (FFFF)

Figure 26: Plates with three different boundary conditions.

range aligns well with the frequency range of dynamic response attenuation observed in the full-scale structure with different boundary conditions, regardless of whether fluid-induced added mass effects are considered. However, anti-resonance points are evident in all the frequency responses with clamped boundaries. The term "anti-resonance point" numerically indicates a complete cancellation of structure vibrations, which is challenging to achieve in experiments, although this phenomenon is commonly observed in other research [32, 34, 35, 36]. From the frequency response results, it is apparent that these anti-resonance points are more likely attributable to the choice of plate boundaries. Changing from clamped to simply supported and free boundaries reduces the constrained degrees of freedom on the boundaries, resulting in fewer anti-resonance points within the amplitude attenuation range. Nevertheless, complete elimination of anti-resonance points through changes in plate boundary conditions is not achievable. Additionally, considering that clamped boundaries are difficult to realise in a laboratory environment, we would recommend using simply supported or free boundaries for the composite plate.

The overall consistency between bandgap predictions of single unit cell and frequency responses of full-scale structure shows the effectiveness of the bandgap analysis in predicting dynamic behaviours of composite plates in both fluid-free and fluid-structure interaction scenarios. Moreover, the approach exhibits good versatility in its application to composite plates with different inclusion shapes, confirming its potential for exploring and optimising a wide range of composite structures with varying geometric

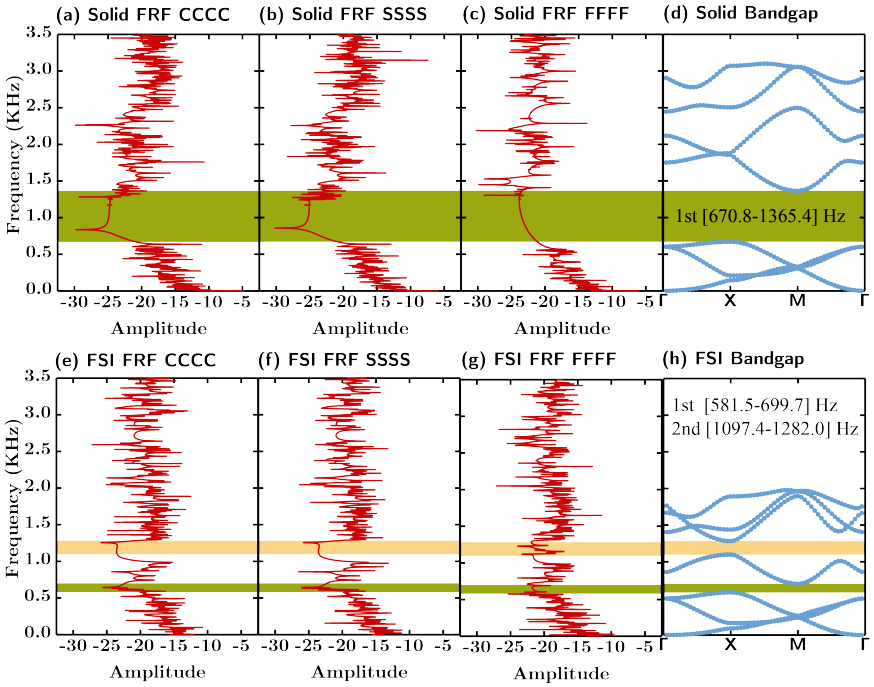

Figure 27: The comparison between the bandgap and the frequency responses for the periodic composite plate with square inclusion with different boundary conditions.

configurations. Through comparison of the dynamic behaviours of the composite plate with and without the fluid environment, we see a significant impact on the dynamic response of the composite plate by fluid-structure interaction. This confirms the importance of accounting for fluid-structure interaction in the design and analysis of composite structures for applications involving fluids.

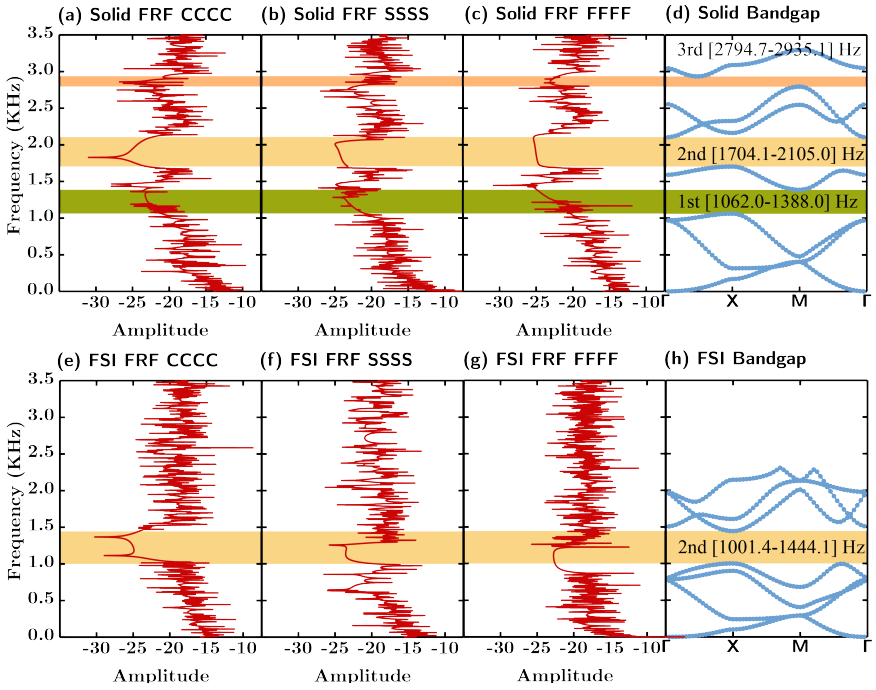

Figure 28: The comparison between the bandgap and the frequency responses for the periodic composite plate with octagonal star inclusion with different boundary conditions

6 Conclusion

This work has investigated a unit cell-based finite element model for predicting the vibration bandgaps of composite plates in the context of fluid-structure interaction (FSI). The approach utilises a unit cell FSI system composed of fluid and solid domains with boundaries incorporating Bloch periodic conditions, enabling vibration bandgap analysis. The effective inertial effect resulting from fluid-structure interaction is described by an added mass matrix, which integrates Bloch periodic conditions for bandgap calculations. The composite plate, modeled using Mindlin kinematics, shares a discretised interface with the fluid domain, where integration leads to the calculation of the added mass. Results indicate that the presence of fluids has a considerable effect on structural vibration, with parameters such as fluid density significantly affecting the bandgap range and position. Additionally, the study demonstrates that the depth of the fluid domain has little impact on structural vibration when the effect of gravity is not considered. While FSI conditions have a negligible effect on vibration mode shape, their consideration significantly affects the inertial mass of the structure and the wave propagation outside the bandgap range.

To further evaluate the method and prepare for future experimental research, full-scale models are employed using frequency response simulations with frequency response functions (FRFs), which are then compared with bandgap predictions. Here, simply supported or unconstrained boundary conditions have been considered for the full-scale model to minimise anti-resonance points in the wave attenuation range. The comparison results indicated the effectiveness of the approach, allowing for the design of composite plates that operate under FSI conditions with specific requirements regarding vibration behaviours.

However, we acknowledge that the method presented in this study becomes less suitable in the ultra high-frequency domain. This limitation arises from the necessity of utilizing a significantly dense mesh

to accurately capture wave propagations with very small wavelengths, which may result in unacceptable computational costs. Moreover, when considering scenarios involving unconstrained fluid surfaces or compressible fluid assumptions, which go beyond the inertial FSI conditions, specific FSI models accounting for fluid gravity and compressibility will be necessary. Nevertheless, the methodology allowing for the integration of periodic boundary conditions in the context of unit cell-based bandgap analysis still holds. Therefore, in perspective, efforts in applying further FSI models are necessary to extend the applicability of this methodology to a broader range of applications.

Acknowledgments

This work was supported by the China Scholarship Council (CSC No. 202106050012).

Appendix A

Solid domain: Mindlin plate finite element

The solid domain, denoted by Ω_s, is characterised by a periodic composite plate structure in the current study. We employ a 4-node plate finite element involving 12 degrees of freedom, and compatible with the Mindlin kinematics assumptions to discretise Ω_s. In this specific study, we investigate a plate of thickness h h, subjected to concentrated or distributed out-of-plane force load $\mathcal{F}3$ along the $\boldsymbol{x}3$ axis and in-plane couple loads (pure moments) $\mathcal{M}1$ and $\mathcal{M}2$ applied relative to the $\boldsymbol{x}_1$ and $\boldsymbol{x}_2$ axes, as illustrated in Figure A.1. The 3D kinematics of the Mindlin plate can be described by the displacement vectors $u_1(x_1, x_2, x_3)$, $u_2(x_1, x_2, x_3)$, and $u_3(x_1, x_2, x_3)$, defined on a point (x_1, x_2, x_3) belonging to Ω_s. Regarding the kinematics of the plate middle plane ($x_3 = 0$), it is described by three kinematics variables: the out-of-plane displacement $w(x_1, x_2)$, and the rotation angles of the normal vector, denoted $\phi_1(x_1, x_2)$ and $\phi_2(x_1, x_2)$, defined around the $\boldsymbol{x}_1$ and $\boldsymbol{x}_2$ axes, respectively.

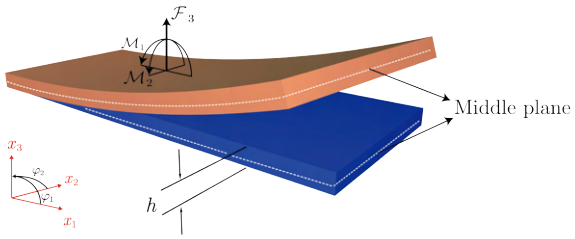

Figure A.1: Mindlin plate kinematics: initial and deformed configurations.

Employing these parameters, we formulate fundamental kinematic relationships that respect the classical Mindlin plate assumptions [29], implying that the plate cross-section remains flat but does not necessarily remain perpendicular to the mid-plane during deformation. Moreover, in-plane stretching is disregarded in light of the vibration analysis, where the out-of-plane movements are predominant. Consequently, the 3D displacement field of Ω_s can be described in terms of the middle plane kinematics

variables $w(x_1, x_2)$, $\phi_1(x_1, x_2)$ and $\phi_2(x_1, x_2)$ as:

$$\begin{aligned} u_1(x_1, x_2, x_3) &= -x_3\phi_1(x_1, x_2) \\ u_2(x_1, x_2, x_3) &= -x_3\phi_2(x_1, x_2) \\ u_3(x_1, x_2, x_3) &= w(x_1, x_2) \end{aligned} \quad , \tag{A.1}$$

with $w(x_1, x_2)$, $\phi_1(x_1, x_2)$ and $\phi_2(x_1, x_2)$, the nodal degrees of freedom of the Mindlin plate finite element, again defined on the plate middle plane. Substituting the Mindlin plate kinematics relation Eq. (A.1) into Eq. (3), we obtain the expression of the Cauchy strain vector $\{\boldsymbol{\varepsilon}\}$ as

$$\{\boldsymbol{\varepsilon}\} = \begin{Bmatrix} \varepsilon_{11} \\ \varepsilon_{22} \\ \gamma_{12} \\ \hdashline \gamma_{13} \\ \gamma_{23} \end{Bmatrix} = \begin{Bmatrix} -x_3 \frac{\partial \phi_1}{\partial x_1} \\ -x_3 \frac{\partial \phi_2}{\partial x_2} \\ -x_3 \left(\frac{\partial \phi_1}{\partial x_2} + \frac{\partial \phi_2}{\partial x_1} \right) \\ \hdashline \frac{\partial w}{\partial x_1} - \phi_1 \\ \frac{\partial w}{\partial x_2} - \phi_2 \end{Bmatrix} = \begin{Bmatrix} \boldsymbol{\varepsilon}_b \\ \hdashline \boldsymbol{\varepsilon}_s \end{Bmatrix} , \tag{A.2}$$

in which in-plane and out-of-plane strain components are denoted distinctly as $\{\boldsymbol{\varepsilon}_b\}$ and $\{\boldsymbol{\varepsilon}_s\}$, respectively, which are associated with the effects of bending and transverse shear. To decouple the bending strain components from their dependence on x_3, we can define the generalised strain $\hat{\boldsymbol{\varepsilon}}$ for the Mindlin plate as follows:

$$\{\hat{\boldsymbol{\varepsilon}}\} = \begin{Bmatrix} \hat{\boldsymbol{\varepsilon}}_b \\ \hdashline \hat{\boldsymbol{\varepsilon}}_s \end{Bmatrix} = \begin{Bmatrix} \frac{\partial \phi_1}{\partial x_1} \\ \frac{\partial \phi_2}{\partial x_2} \\ \frac{\partial \phi_1}{\partial x_2} + \frac{\partial \phi_2}{\partial x_1} \\ \hdashline \frac{\partial w}{\partial x_1} - \phi_1 \\ \frac{\partial w}{\partial x_2} - \phi_2 \end{Bmatrix} , \tag{A.3}$$

using $\{\boldsymbol{\varepsilon}\} = [\mathbf{S}_\varepsilon]\{\hat{\boldsymbol{\varepsilon}}\}$, with the transformation matrix $[\mathbf{S}_\varepsilon]$ that factorises the coordinate x_3

$$[\mathbf{S}_\varepsilon] = \mathrm{diag}\,[-x_3 \quad -x_3 \quad -x_3 \quad 1 \quad 1\ ] \ . \tag{A.4}$$

In the subsequent discussion, we present the finite element interpolation technique, which leads to matrix expressions of $\boldsymbol{\varepsilon}$ and $\hat{\boldsymbol{\varepsilon}}$ as functions of nodal degrees of freedom $(w, \phi_1, \phi_2)_i$, where $i = 1, ..., 4$.

Finite element interpolation: Referring to Eq. (A.1), the Mindlin finite element employs four nodal kinematic variables, resulting in the nodal displacement vector:

$$\{\mathbf{u}_i\} = \begin{bmatrix} w & \phi_1 & \phi_2 \end{bmatrix}_i , \quad i = 1, ..., 4 \ . \tag{A.5}$$

For a 4-node element, this leads to the element displacement vector:

$$\{\mathbf{u}\}_{12\times 1} = \begin{bmatrix} \{\mathbf{u}_1\}, & \{\mathbf{u}_2\}, & \{\mathbf{u}_3\}, & \{\mathbf{u}_4\} \end{bmatrix}^{\mathrm{T}} \ . \tag{A.6}$$

Hence, the approximation of the displacement field for the 4-node Mindlin plate element is expressed

using linear shape functions in the reference element of domain $[-1,1]\times[-1,1]$:

$$w=\sum_{i=1}^{4}N_{si}w_i,\qquad \phi_1=\sum_{i=1}^{4}N_{si}\phi_{1i},\qquad \phi_2=\sum_{i=1}^{4}N_{si}\phi_{2i},\ . \tag{A.7}$$

with

$$N_{si}=\frac{1}{4}\left(1+\xi_i\xi_n\right)\left(1+\eta_i\eta_n\right)\ \ , \tag{A.8}$$

where (ξ_i,η_i) with $i=1,2,3,4$ represent the positions of the i-th node in the parametric coordinates, and (ξ_n,η_n) represents the position within the reference element.

Element stiffness matrix and mass matrix: Using the shape functions (Eq. (A.8)), we can present the strain-displacement matrix $[\mathbf{B}_s]$ by considering the expression of the generalised strain $\{\hat{\boldsymbol{\varepsilon}}\}$ (Eq. (A.3)) and the element vector of displacement $\{\mathbf{u}\}$ (Eq. (A.6)):

$$[\mathbf{B}_s]=\begin{bmatrix} 0 & \frac{\partial N_{s1}}{\partial x_1} & 0 & & 0 & \frac{\partial N_{s4}}{\partial x_1} & 0\\ 0 & 0 & \frac{\partial N_{s1}}{\partial x_2} & & 0 & 0 & \frac{\partial N_{s4}}{\partial x_2}\\ 0 & \frac{\partial N_{s1}}{\partial x_2} & \frac{\partial N_{s1}}{\partial x_1} & \cdots & 0 & \frac{\partial N_{s4}}{\partial x_2} & \frac{\partial N_{s4}}{\partial x_1}\\ \frac{\partial N_{s1}}{\partial x_1} & -N_{s1} & 0 & & \frac{\partial N_{s4}}{\partial x_1} & -N_{s4} & 0\\ \frac{\partial N_{s1}}{\partial x_2} & 0 & -N_{s1} & & \frac{\partial N_{s4}}{\partial x_2} & 0 & -N_{s4} \end{bmatrix}\ , \tag{A.9}$$

which leads to

$$\{\hat{\boldsymbol{\varepsilon}}\}=[\mathbf{B}_s]\,\{\mathbf{u}\}\ . \tag{A.10}$$

The element stiffness matrix $[\mathbf{k}_s^e]$ can be determined by using the strain-displacement matrix $[\mathbf{B}_s]$ (Eq. (A.9)) in consideration of linear elasticity with the constitutive relation:

$$[\mathbf{k}_s^e]=\int_{\Omega_{se}}[\mathbf{B}_s]^{\mathrm{T}}\left[\hat{\mathbf{C}}\right][\mathbf{B}_s]\ \mathrm{d}\Omega_{se}\ , \tag{A.11}$$

in which Ω_{se} refers to the middle plane area of the Mindlin plate element e, and $\left[\hat{\mathbf{C}}\right]$, the generalised elasticity matrix for the Mindlin plate, can be obtained by integration across the plate thickness h using $\left[\hat{\mathbf{C}}\right]$, the generalised elasticity matrix for the Mindlin plate:

$$\left[\hat{\mathbf{C}}\right]=\int_{-\frac{h}{2}}^{\frac{h}{2}}[\mathbf{S}_\varepsilon]^{\mathrm{T}}[\mathbf{C}][\mathbf{S}_\varepsilon]\,\mathrm{d}x_3\ \ , \tag{A.12}$$

based on linear elasticity, which for plane stress assumption, writes

$$[\mathbf{C}]=\begin{bmatrix} \frac{E}{1-v^2} & \frac{vE}{1-v^2} & 0 & 0 & 0\\ \frac{vE}{1-v^2} & \frac{E}{1-v^2} & 0 & 0 & 0\\ 0 & 0 & \cancel{\frac{E}{2(1+v)}}\ G & 0 & 0\\ 0 & 0 & 0 & k_{11}G & 0\\ 0 & 0 & 0 & 0 & k_{22}G \end{bmatrix}\ . \tag{A.13}$$

Here, E refers to Young's modulus, v is Poisson's ratio, G is the shear modulus, and k_{11}, k_{22} are in plane shear correction parameters, which in this article, take the following value $k_{11}=k_{22}=\frac{5}{6}$.

In a similar manner, we can construct the element mass matrix $[\mathbf{m}_s^e]$ using the plate density matrix $[\boldsymbol{\rho}_s]$, which arises from integrating the material unit mass and inertia over the plate thickness (h). With:

$$[\boldsymbol{\rho}_s] = \int_{-\frac{h}{2}}^{\frac{h}{2}} \begin{bmatrix} \rho_s & 0 & 0 \\ 0 & \rho_s {x_3}^2 & 0 \\ 0 & 0 & \rho_s {x_3}^2 \end{bmatrix} \mathrm{d}x_3 \ , \tag{A.14}$$

we obtain the element mass matrix $[\mathbf{m}_s^e]$ for the element e as:

$$[\mathbf{m}_s^e] = \int_{\Omega_{se}} [\mathbf{N}_s]^{\mathrm{T}} [\boldsymbol{\rho}_s] [\mathbf{N}_s] \ \mathrm{d}\Omega_{se} \ , \tag{A.15}$$

where the matrix of shape functions $[\mathbf{N}_s]$, composed of Eq. (A.8) writes

$$[\mathbf{N}_s] = \begin{bmatrix} N_{s1} & 0 & 0 & & N_{s4} & 0 & 0 \\ 0 & N_{s1} & 0 & \cdots & 0 & N_{s4} & 0 \\ 0 & 0 & N_{s1} & & 0 & 0 & N_{s4} \end{bmatrix} . \tag{A.16}$$

Global stiffness matrix and mass matrix: Let us introduce the element localisation matrix $[\boldsymbol{\Lambda}_s^e]$ for the solid domain. This matrix, of dimension $12 \times \mathrm{NDOF}_{\mathrm{global}}$, establishes the correspondance between the indices of the element degrees of freedom and their respective positions within the global system. In numerical implementation, this process can be achieved through the assembly operation. This leads to the expression of the global stiffness and mass matrices of the solid domain Ω_s, $[\mathbf{K}_s]$ and $[\mathbf{M}_s]$, which are given by:

$$\begin{aligned} [\mathbf{K}_s] &= \sum_{e=1}^{\mathrm{NE}_s} [\boldsymbol{\Lambda}_s^e]^{\mathrm{T}} [\mathbf{k}_s^e] [\boldsymbol{\Lambda}_s^e] \\ [\mathbf{M}_s] &= \sum_{e=1}^{\mathrm{NE}_s} [\boldsymbol{\Lambda}_s^e]^{\mathrm{T}} [\mathbf{m}_s^e] [\boldsymbol{\Lambda}_s^e] \end{aligned} \ , \tag{A.17}$$

where $[\mathbf{k}_s^e]$ and $[\mathbf{m}_s^e]$ represent the element stiffness and mass matrices, obtained from Eq. (A.11) and Eq. (A.15), respectively. Utilising the expressions of the global stiffness and mass matrices, we can formulate the matrix representation that implements the elastodynamics of the solid domain Ω_s, which corresponds to the left-hand side of Eq. (12), as follows:

$$\begin{aligned} \int_{\Omega_s} \boldsymbol{\sigma} : \delta\boldsymbol{\varepsilon} \mathrm{d}\Omega_s \quad &\rightarrow \quad \{\delta\mathbf{U}\}^{\mathrm{T}} [\mathbf{K}_s] \{\mathbf{U}\} \\ \int_{\Omega_s} \rho_s \ddot{\boldsymbol{u}} \cdot \delta\boldsymbol{u} \Omega_s \quad &\rightarrow \quad \{\delta\mathbf{U}\}^{\mathrm{T}} [\mathbf{M}_s] \left\{\ddot{\mathbf{U}}\right\} \end{aligned} . \tag{A.18}$$

The boundary conditions applied on Ω_s, which are exerted through the fluid-structure interface and described by the right-hand side of the governing equation Eq. (12), require integration over the fluid-structure interface. A comprehensive discussion on this aspect will be presented in Section 3.1.

Appendix B

Fluid domain: 8-node hexahedral finite element

In this section, we focus on the finite element formulation that implements the wave equation in terms of the pressure fluctuation of Ω_f relative to its steady state. We consider Ω_f filled with a weakly compressible, non-viscous fluid without body forces whose pressure fluctuation is described by the Laplace equation (Eq. (8)). The domain is discretised using a 8-node hexahedral finite element, for which the nodal pressure p is the sole degree of freedom. We construct the element vector of pressure as follows:

$$\{\mathbf{p}\}_{8\times 1} = \begin{bmatrix} p_1 & p_2 & p_3 & p_4 & p_5 & p_6 & p_7 & p_8 \end{bmatrix}^{\mathrm{T}} \quad . \tag{B.1}$$

The pressure field is approximated by interpolating nodal pressures through linear shape functions in the reference element of domain $[-1,1]\times[-1,1]\times[-1,1]$, resulting in the expression:

$$p = \sum_{i=1}^{8} N_{fi} p_i \quad . \tag{B.2}$$

Here, the shape function is defined as:

$$N_{fi} = \frac{1}{8}\left(1+\xi_i\xi_n\right)\left(1+\eta_i\eta_n\right)\left(1+\lambda_i\lambda_n\right) \quad , \tag{B.3}$$

where $(\xi_i, \eta_i, \lambda_i)$ with $i = 1, 2, 3, ..., 8$ represents the positions of the i-th node in the parametric coordinates, and $(\xi_n, \eta_n, \lambda_n)$ represents the position within the reference element. Using the shape functions (Eq. (B.3)), we can write the shape function gradients matrix $[\mathbf{B}_f]$:

$$[\mathbf{B}_f] = \begin{bmatrix} \frac{\partial N_{f1}}{\partial x_1} & \frac{\partial N_{f2}}{\partial x_1} & \cdots & \frac{\partial N_{f8}}{\partial x_1} \\ \frac{\partial N_{f1}}{\partial x_2} & \frac{\partial N_{f2}}{\partial x_2} & \cdots & \frac{\partial N_{f8}}{\partial x_2} \\ \frac{\partial N_{f1}}{\partial x_3} & \frac{\partial N_{f2}}{\partial x_3} & & \frac{\partial N_{f8}}{\partial x_3} \end{bmatrix} \quad , \tag{B.4}$$

which leads to:

$$\{\nabla p\} = [\mathbf{B}_f]\{\mathbf{p}\} \quad . \tag{B.5}$$

We can construct the element stiffness matrix $\left[\mathbf{k}_f^e\right]$ for the fluid domain, which represents the linearised elastic properties of the fluid. Holding the assumptions that for the weakly compressible ideal fluid initially at rest, the perturbation of the fluid pressure is supposed to be small with respect to the steady state. Under these conditions, the linearised elastic properties of the fluid imply that the fluid pressure field responds linearly to an external vibroacoustic load, characterised by the fluid stiffness matrix. By considering the governing equation of the fluid domain Eq. (13), we obtain the expression of $\left[\mathbf{k}_f^e\right]$ for the $e-$th element of the fluid domain as:

$$\left[\mathbf{k}_f^e\right] = \int_{\Omega_{fe}} [\mathbf{B}_f]^{\mathrm{T}} [\mathbf{B}_f] \ \mathrm{d}\Omega_{fe} \quad , \tag{B.6}$$

where Ω_{fe} refers to the volume of the element. Subsequently, we proceed with the assembly operation by using the element localisation matrix $\left[\mathbf{\Lambda}_f^e\right]$, defined similarly as for the solid domain. Here, $\left[\mathbf{\Lambda}_f^e\right]$ is of dimensions $8 \times \mathrm{NDOF}_{\mathrm{global}}$ and allows relating the indices of the element degrees of freedom to their

respective positions within the global system. Consequently, the global stiffness matrix for the fluid domain can be obtained based on Eq. (B.6) as follows:

$$[\mathbf{K}_f] = \sum_{e=1}^{\mathrm{NE}_f} \left[\mathbf{\Lambda}_f^e\right]^{\mathrm{T}} \left[\mathbf{k}_f^e\right] \left[\mathbf{\Lambda}_f^e\right] \quad , \tag{B.7}$$

Based on the global stiffness matrix, we can construct the matrix formulation to solve the pressure fluctuation of the fluid domain Ω_f. This formulation corresponds to the left-hand side of Eq. (13) and can be expressed as:

$$\int_{\Omega_f} \nabla p \cdot \nabla \delta p \, \mathrm{d}\Omega_f \quad \rightarrow \quad \{\delta \mathbf{P}\}^{\mathrm{T}} [\mathbf{K}_f] \{\mathbf{P}\} \quad , \tag{B.8}$$

where $\{\delta \mathbf{P}\}$ and $\{\mathbf{P}\}$ are the global vectors of the virtual pressure fluctuation, and of the pressure fluctuaton of Ω_f, respectively. The boundary conditions on Ω_f are applied through the fluid-structure interface, and is described by the right-hand side of Eq. (13).

Appendix C

Bloch boundary conditions for bandgap analysis

Due to the periodic nature of the composite plate considered in this study, its microstructure can be described using the 2-dimensional Bravais lattice [37] in real space, as depicted in Figure C.1(a). This lattice is formed by generating an infinite number of translation vectors with integer coefficients:

$$\mathbf{R}_n = n_1 \boldsymbol{a}_1 + n_2 \boldsymbol{a}_2 \quad n_1, n_2 \in \mathbb{Z} \tag{C.1}$$

where vectors $\boldsymbol{a}_1$ and $\boldsymbol{a}_2$ are lattice vectors in two periodic directions, considering the 2-dimensional periodicity. The lattice points repeat endlessly in all periodic directions, making it challenging to represent the entire lattice with limited computational resources. Therefore, adopting the periodicity of the lattice, it is sufficient to only identify one period. This region is a parallelogram represented in Figure C.1(a) and is also called the primitive unit cell, which is a square in a square Bravais lattice. Subsequently, the entire Bravais lattice can be generated by using translations only.

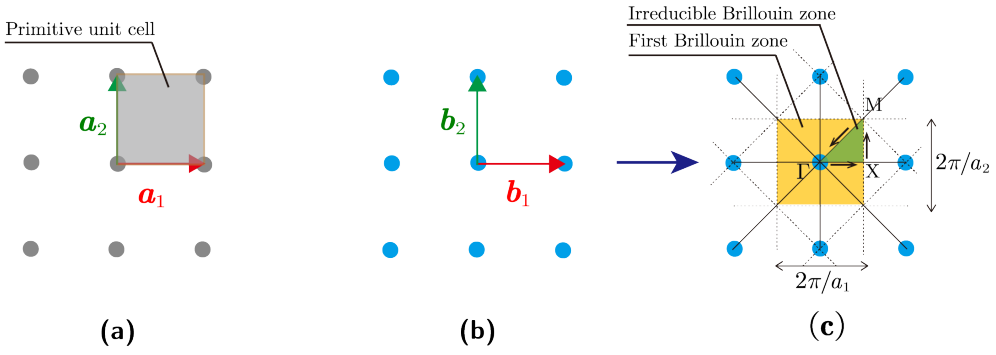

Figure C.1: The square Bravais lattice in real space (a), the reciprocal lattice in reciprocal space (b), and Brillouin zone (c).

Applying a Fourier transform of the geometric lattice (Bravais lattice) yields a lattice system in reciprocal space, as depicted in Figure C.1(b). To illustrate the reciprocal space, consider a function

$\mathbf{u}_k(\mathbf{x})$ following the periodicity of the Bravais lattice, which can be expressed as a multi-dimensional Fourier series:

$$\mathbf{u}_k\left(\mathbf{x}\right) = \sum_{\mathbf{G}_m} f_{\mathbf{G}_m} e^{\mathrm{i}\mathbf{G}_m \cdot \mathbf{x}} \tag{C.2}$$

where $f_{\mathbf{G}_m}$ represents the Fourier coefficients associated with the reciprocal lattice vector $\mathbf{G}_m$. Then, translating the space vector $\mathbf{x}$ by any lattice vector $\mathbf{R}_n$, the function $\mathbf{u}_k(\mathbf{x}+\mathbf{R}_n)$ will be equal to $\mathbf{u}_k(\mathbf{x})$:

$$\begin{aligned}
\mathbf{u}_k\left(\mathbf{x}\right) &= \mathbf{u}_k\left(\mathbf{x} + \mathbf{R}_n\right) \\
\sum_{\mathbf{G}_m} f_{\mathbf{G}_m} e^{\mathrm{i}\mathbf{G}_m \cdot \mathbf{x}} &= \sum_{\mathbf{G}_m} f_{\mathbf{G}_m} e^{\mathrm{i}\mathbf{G}_m \cdot (\mathbf{x}+\mathbf{R}_n)} \\
\sum_{\mathbf{G}_m} f_{\mathbf{G}_m} e^{\mathrm{i}\mathbf{G}_m \cdot \mathbf{x}} &= \sum_{\mathbf{G}_m} f_{\mathbf{G}_m} e^{\mathrm{i}\mathbf{G}_m \cdot \mathbf{x}} e^{\mathrm{i}\mathbf{G}_m \cdot \mathbf{R}_n} \\
e^{\mathrm{i}\mathbf{G}_m \cdot \mathbf{R}_n} &= 1 \\
\mathbf{G}_m \cdot \mathbf{R}_n &= 2\pi N \quad N \in \mathbb{Z}
\end{aligned} \tag{C.3}$$

Mathematically, the reciprocal lattice is the set of all 2-dimensional reciprocal lattice vectors $\mathbf{G}_m$, which are wave vectors of plane waves in the Fourier series of a spatial function whose periodicity is the same as that of the Bravais lattice (the set of all Bravais lattice point position vectors $\mathbf{R}_n$):

$$\mathbf{G}_m = m_1 \boldsymbol{b}_1 + m_2 \boldsymbol{b}_2 \quad m_1, m_2 \in \mathbb{Z} \tag{C.4}$$

where $\boldsymbol{a}_i \cdot \boldsymbol{b}_j = 2\pi\delta_{ij}$, which reveals the mapping relationship between $\mathbf{G}_m$ and $\mathbf{R}_n$. Vectors in the Bravais lattice have dimensions of [length], while vectors in the reciprocal lattice have the dimensions of [1/length].

Similar to the primitive unit cell in real space, there is a region of reciprocal space that contains all the information of the lattice. This region is known as the first Brillouin zone [37], which is the smallest volume entirely enclosed by planes that are the perpendicular bisectors of the reciprocal lattice vectors drawn from the origin, as shown in Figure C.1(c).

The consequences of periodicity are described mathematically by the Bloch's theorem [38], which states that solution of the wave equation (mechanical, electromagnetic, schrodinger, etc.) can be completely characterised by their behaviour in a single Brillouin zone expressed as a periodic function modulated by a plane wave:

$$\boldsymbol{\psi}(\mathbf{x}, \mathbf{k}) = e^{(\mathrm{i}\mathbf{k}\cdot\mathbf{x})} \mathbf{u}_k\left(\mathbf{x}\right) \tag{C.5}$$

where $\mathbf{u}_k$ is the periodic function mentioned earlier, and $\mathbf{k}$ is the wave vector. The calculation of the band structure for the periodic composite plate requires the use of periodicity and symmetry of the crystal lattice, and usually assumes that the crystal is ideal and has periodic boundaries and discrete translational symmetries. Because of this, the band gap is typically plotted only for $\mathbf{k}$ vectors within the first Brillouin zone. The solution of the wave vector outside the first Brillouin zone corresponds to the solution inside. For the solution of elastic wave propagation in a periodic medium, we have:

$$\mathbf{U}(\mathbf{x}, \mathbf{k}) = e^{(\mathrm{i}\mathbf{k}\cdot\mathbf{x})} \mathbf{u}_k\left(\mathbf{x}\right) \tag{C.6}$$

Similarly, we consider the translation of space vector $\mathbf{x}$ by lattice vector $\mathbf{R}_n = n_1 \boldsymbol{a}_1 + n_2 \boldsymbol{a}_2$ with

$n_1 = n_2 = 1$, and obtain the boundary conditions of the mechanical wave of a unit cell in real space:

$$\begin{aligned}\mathbf{U}(\mathbf{x}+\boldsymbol{a}_i,\mathbf{k}) &= e^{\mathrm{i}(\mathbf{k}\cdot(\mathbf{x}+\boldsymbol{a}_i))}\mathbf{u}_k(\mathbf{x}) \\ &= e^{\mathrm{i}(\mathbf{k}\cdot\boldsymbol{a}_i)}e^{\mathrm{i}(\mathbf{k}\cdot\mathbf{x})}\mathbf{u}_k(\mathbf{x}) \\ &= e^{\mathrm{i}(\mathbf{k}\cdot\boldsymbol{a}_i)}\mathbf{U}(\mathbf{x},\mathbf{k})\end{aligned} \tag{C.7}$$

which respects the Bloch theorem. In general, high-symmetry points in the first Brillouin zone are often associated with energy level degeneracy and reflect the lattice symmetry. Therefore, the band structure diagram is typically presented along high-symmetry points [39]. The high-symmetry points in the first Brillouin zone of a square reciprocal lattice are often denoted as Γ, X, M, as shown in Figure C.1(c). The Bloch wave vectors $\mathbf{k}$ in Eq. (C.5) will be further simplified within the path formed by the connection of high-symmetrical points $\Gamma-\mathrm{X}-\mathrm{M}-\Gamma$, where the region inside the path is the irreducible Brillouin zone. For each $\mathbf{k}$ on the path, the wave equation with the boundary condition Eq. (C.7) will have multi solutions for the characteristic frequencies. The number of solutions are also the number of band branches. Each band changes periodically with $\mathbf{k}$.

Appendix D

Consider the free vibration of an undamped finite solid structure. The equation of motion for this structure can be solved using finite element method, for which the governing equation in matrix form writes:

$$[\mathbf{M}_s]\left\{\ddot{\mathbf{U}}\right\} + [\mathbf{K}_s]\{\mathbf{U}\} = 0 \tag{D.1}$$

It should be noted that the Bloch boundary conditions are not involved in this equation as they are only applied for the unit cell system. For such a solid system without external force, the displacement solution of Eq. (D.1) can be expressed in a harmonic form, $\{\mathbf{U}\} = \{\mathbf{U}_0\}e^{\mathrm{i}\omega t}$. Then Eq. (D.1) can be rewritten as:

$$\left([\mathbf{K}_s] - \omega^2[\mathbf{M}_s]\right)\{\mathbf{U}_0\}e^{\mathrm{i}\omega t} = \left([\mathbf{K}_s] - \omega^2[\mathbf{M}_s]\right)\{\mathbf{U}\} = 0 \tag{D.2}$$

In the case of nontrivial solutions ($\{\mathbf{U}\} \neq 0$), the determinant of the coefficient matrix $\left([\mathbf{K}_s] - \omega^2[\mathbf{M}_s]\right)$ should be zero according to Cramer's Rule. Therefore, the natural frequencies $\{\boldsymbol{\omega}\}$ of the solid structure can be obtained. It should be noted that the number of natural frequencies of a structure is, in fact, equal to the number of DOFs, denoted as $\mathrm{N_{dof}}$. However, in general, we only consider the first few natural frequencies of the structure, denoted as N_ω.

Substituting the rth natural frequency ω_r back into Eq. (D.2) yields the corresponding rth mode shape of the structure, denoted as $\{\boldsymbol{\Phi}_r\}$. After that, all N_ω orders of mode shapes are combined into a mode matrix $[\boldsymbol{\Phi}] = [\{\boldsymbol{\Phi}_1\},\{\boldsymbol{\Phi}_2\},...,\{\boldsymbol{\Phi}_{\mathrm{N}_\omega}\}]_{\mathrm{N_{dof}}\times\mathrm{N}_\omega}$. For a linear vibration solid system, the solution of the displacement field can be written as a linear combination of mode shapes:

$$\{\mathbf{U}\} \approx [\boldsymbol{\Phi}]\{\mathbf{q}\} \tag{D.3}$$

where $\{\mathbf{q}\}_{\mathrm{N}_\omega\times 1}$ denotes the amplitudes of mode shapes. The approximate relationship is used in Eq. (D.3) since not all the characteristic modes of the solid system are employed.

Then, we further consider the mentioned undamped finite solid structure subjected to an external

force. The governing equation of this forced vibration solid system in matrix form can be written as:

$$[\mathbf{M}_s]\left\{\ddot{\mathbf{U}}\right\} + [\mathbf{K}_s]\{\mathbf{U}\} = \{\mathbf{F}\} \tag{D.4}$$

If the external force is harmonic, $\{\mathbf{F}\} = \{\mathbf{F_0}\}\, e^{\mathrm{i}\omega t}$, which will stimulate the structure to generate harmonic displacement response: $\{\mathbf{U}\} = \{\mathbf{U_0}\}\, e^{\mathrm{i}\omega t}$. Therefore, Eq. (D.4) can be rewritten as:

$$\left([\mathbf{K}_s] - \omega^2 [\mathbf{M}_s]\right)\{\mathbf{U}_0\}\, e^{\mathrm{i}\omega t} = \left([\mathbf{K}_s] - \omega^2 [\mathbf{M}_s]\right)\{\mathbf{U}\} = \{\mathbf{F}\} \tag{D.5}$$

For Eq. (D.5), the number of unknowns is equal to the number of dofs of the solid structure $\mathrm{N_{dof}}$. However, by substituting Eq. (D.3) to Eq. (D.5), the the number of unknowns will be reduced to the number of modes N_ω:

$$\left([\mathbf{K}_s] - \omega^2 [\mathbf{M}_s]\right)[\mathbf{\Phi}]\{\mathbf{q}\} = \{\mathbf{F}\} \tag{D.6}$$

Due to the orthogonality of the modes to the mass and stiffness matrices of the structure, the decoupling of the motion equations is achieved by left-multiplying Eq. (D.6) by the matrix $[\mathbf{\Phi}]^{\mathrm{T}}$:

$$\left([\mathbf{\Phi}]^{\mathrm{T}}[\mathbf{K}_s][\mathbf{\Phi}] - \omega^2 [\mathbf{\Phi}]^{\mathrm{T}}[\mathbf{M}_s][\mathbf{\Phi}]\right)\{\mathbf{q}\} = [\mathbf{\Phi}]^{\mathrm{T}}\{\mathbf{F}\} \tag{D.7}$$

where $[\mathbf{\Phi}]^{\mathrm{T}}[\mathbf{M}_s][\mathbf{\Phi}]$ is the mode mass matrix $[\boldsymbol{m}_s] = \mathrm{diag}\begin{bmatrix} m_{s,1} & m_{s,2} & \dots & m_{s,N_\omega} \end{bmatrix}$, and $[\mathbf{\Phi}]^{\mathrm{T}}[\mathbf{K}_s][\mathbf{\Phi}]$ is the mode stiffness matrix $[\boldsymbol{k}_s] = \mathrm{diag}\begin{bmatrix} k_{s,1} & k_{s,2} & \dots & k_{s,N_\omega} \end{bmatrix}$. Therefore, with this decoupled equation, the solution of amplitude of mode shapes $\{\mathbf{q}\}$ can be given:

$$\{\mathbf{q}\} = \left([\boldsymbol{k}_s] - \omega^2 [\boldsymbol{m}_s]\right)^{-1}[\mathbf{\Phi}]^{\mathrm{T}}\{\mathbf{F}\} \tag{D.8}$$

And specifically, the rth order of amplitude of mode shapes q_r is written as:

$$\mathrm{q}_r = \frac{\{\mathbf{\Phi}_r\}^{\mathrm{T}}\{\mathbf{F}\}}{k_{s,r} - \omega^2 m_{s,r}} \tag{D.9}$$

where $\{\mathbf{\Phi}_r\}$ is the rth mode shape of the structure. After that, by combining Eq. (D.3) and (D.8) the stimulated displacement field $\{\mathbf{U}\}$ is given as follow:

$$\{\mathbf{U}\} = \left(\sum_{r=1}^{\mathrm{N}_\omega} \frac{\{\mathbf{\Phi}_r\}\{\mathbf{\Phi}_r\}^{\mathrm{T}}}{k_{s,r} - \omega^2 m_{s,r}}\right)\{\mathbf{F}\} \tag{D.10}$$

This equation indicates the process of force input and response out of a linear undamped solid structure system, and we denote the Frequency Response Function (FRF) transfer matrix $[\mathbf{H}]$ as:

$$[\mathbf{H}] = \sum_{r=1}^{\mathrm{N}_\omega} \frac{\{\mathbf{\Phi}_r\}\{\mathbf{\Phi}_r\}^{\mathrm{T}}}{k_{s,r} - \omega^2 m_{s,r}} \tag{D.11}$$

where $[\mathbf{H}]$ has the matrix size of $\mathrm{N_{dof}} \times \mathrm{N_{dof}}$; ω denotes the frequency of harmonic force. The components of the transfer matrix, H_{ij}, can be physically interpreted as the dynamic response measured on the ith degree of freedom in relation to an input excitation prescribed on the jth degree of freedom. In case of a solid structure coupled with ideal liquid, we just need to replace the mass matrix $[\mathbf{M}_s]$ of solid structure in Eq. (D.1) and (D.4) by $([\mathbf{M}_s] + [\mathbf{M}_A])$, where $[\mathbf{M}_A] = \rho_f [\mathbf{R}][\mathbf{K}_f]^{-1}[\mathbf{R}]^{\mathrm{T}}$.

References

[1] Z. X. Xia, G. Y. Zhang, Y. Cong, S. T. Gu, A non-classical couple stress based mindlin plate finite element framework for tuning band gaps of periodic composite micro plates, Journal of Sound and Vibration 529 (2022) 116889. doi:10.1016/j.jsv.2022.116889.
URL http://dx.doi.org/10.1016/j.jsv.2022.116889

[2] X. Q. Zhou, D. Y. Yu, X. Shao, S. Wang, Y. H. Tian, Band gap characteristics of periodically stiffened-thin-plate based on center-finite-difference-method, Thin-Walled Structures 82 (2014) 115–123. doi:10.1016/j.tws.2014.04.010.
URL http://dx.doi.org/10.1016/j.tws.2014.04.010

[3] C. Gao, D. Halim, X. Yi, Study of bandgap property of a bilayer membrane-type metamaterial applied on a thin plate, International Journal of Mechanical Sciences 184 (2020) 105708. doi:10.1016/j.ijmecsci.2020.105708.
URL http://dx.doi.org/10.1016/j.ijmecsci.2020.105708

[4] F. Liang, Y. Chen, D. Guan, J. Li, Low-frequency band gap characteristics of a novel spinning metamaterial pipe with timoshenko model, Journal of Sound and Vibration 541 (2022) 117316. doi:10.1016/j.jsv.2022.117316.
URL https://doi.org/10.1016/j.jsv.2022.117316

[5] A. K. Singh, S. P. Singh, Band-gap-tailoring in liquid crystals: Organizing metal atoms and nanoclusters in lc media, Liquid Crystals 49 (5) (2021) 605–632. doi:10.1080/02678292.2021.1993457.
URL http://dx.doi.org/10.1080/02678292.2021.1993457

[6] S. Carra, M. Amabili, R. Ohayon, P. M. Hutin, Active vibration control of a thin rectangular plate in air or in contact with water in presence of tonal primary disturbance, Aerospace Science and Technology 12 (1) (2008) 54–61. doi:10.1016/j.ast.2007.10.001.
URL https://doi.org/10.1016/j.ast.2007.10.001

[7] W. Larbi, J.-F. Deü, R. Ohayon, Finite element reduced order model for noise and vibration reduction of double sandwich panels using shunted piezoelectric patches, Applied Acoustics 108 (2016) 40–49. doi:10.1016/j.apacoust.2015.08.021.
URL https://doi.org/10.1016/j.apacoust.2015.08.021

[8] D. Yu, J. Wen, H. Zhao, Y. Liu, X. Wen, Vibration reduction by using the idea of phononic crystals in a pipe-conveying fluid, Journal of Sound and Vibration 318 (1-2) (2008) 193–205. doi:10.1016/j.jsv.2008.04.009.
URL https://doi.org/10.1016/j.jsv.2008.04.009

[9] O. Thierry, O. D. Smet, J.-F. Deü, Vibration reduction of a woven composite fan blade by piezoelectric shunted devices, Journal of Physics: Conference Series 744 (2016) 012164. doi:10.1088/1742-6596/744/1/012164.
URL https://doi.org/10.1088/1742-6596/744/1/012164

[10] N. Atalla, R. J. Bernhard, Review of numerical solutions for low-frequency structural-acoustic problems, Applied Acoustics 43 (3) (1994) 271–294.

[11] K.-J. Bathe, Finite element method (Jun. 2008). doi:10.1002/9780470050118.ecse159.
URL http://dx.doi.org/10.1002/9780470050118.ecse159

[12] H. Morand, R. Ohayon, Interactions fluides-structures, Recherches en mathématiques appliquées, Masson, 1992.
URL https://books.google.fr/books?id=9hZnPQAACAAJ

[13] J.-F. Sigrist, Fluid-Structure Interaction, Wiley, 2015. doi:10.1002/9781118927762.
URL https://doi.org/10.1002/9781118927762

[14] O. C. Zienkiewicz, R. E. Newton, Coupled vibrations of a structure submerged in a compressible fluid, in: Symposium on Finite Element Techniques at the Institut für Statik und Dynamik der Luft-und Raumfahrtkonstruktionen, University of Stuttgart, Stuttgart, Germany, 1969, report No. C/R/101/69.

[15] J.-F. Sigrist, S. Garreau, Dynamic analysis of fluid–structure interaction problems with modal methods using pressure-based fluid finite elements, Finite Elements in Analysis and Design 43 (4) (2007) 287–300. doi:10.1016/j.finel.2006.10.002.
URL https://doi.org/10.1016/j.finel.2006.10.002

[16] J.-F. Deü, W. Larbi, R. Ohayon, Piezoelectric structural acoustic problems: Symmetric variational formulations and finite element results, Computer Methods in Applied Mechanics and Engineering 197 (19-20) (2008) 1715–1724. doi:10.1016/j.cma.2007.04.014.
URL https://doi.org/10.1016/j.cma.2007.04.014

[17] J.-F. Sigrist, D. Broc, Dynamic analysis of a tube bundle with fluid–structure interaction modelling using a homogenisation method, Computer Methods in Applied Mechanics and Engineering 197 (9-12) (2008) 1080–1099. doi:10.1016/j.cma.2007.10.010.
URL https://doi.org/10.1016/j.cma.2007.10.010

[18] E. Li, Z. C. He, G. Wang, G. R. Liu, An efficient algorithm to analyze wave propagation in fluid/solid and solid/fluid phononic crystals, Computer Methods in Applied Mechanics and Engineering 333 (2018) 421–442. doi:10.1016/j.cma.2018.01.006.
URL https://doi.org/10.1016/j.cma.2018.01.006

[19] M. Cinefra, M. C. Moruzzi, S. Bagassi, E. Zappino, E. Carrera, Vibro-acoustic analysis of composite plate-cavity systems via CUF finite elements, Composite Structures 259 (2021) 113428. doi:10.1016/j.compstruct.2020.113428.
URL https://doi.org/10.1016/j.compstruct.2020.113428

[20] L. N. Brillouin, Wave Propagation in Periodic Structures: Electric Filters and Crystal Lattices, Dover books on engineering and engineering physics, McGraw-Hill Book Company, Incorporated, 1946.
URL https://books.google.fr/books?id=kCUIAQAAIAAJ

[21] E. Li, Z. C. He, G. Wang, Y. Jong, Fundamental study of mechanism of band gap in fluid and solid/fluid phononic crystals, Advances in Engineering Software 121 (2018) 167–177. doi:10.1016/j.advengsoft.2018.04.014.
URL http://dx.doi.org/10.1016/j.advengsoft.2018.04.014

[22] X. Y. Lin, E. Li, Z. C. He, Y. Wu, A novel method to study the phononic crystals with fluid–structure interaction and hybrid uncertainty, Acta Mechanica 231 (1) (2019) 321–352.

doi:10.1007/s00707-019-02530-8.
URL http://dx.doi.org/10.1007/s00707-019-02530-8

[23] J.-H. Wu, Y.-D. Sun, M.-Z. Su, H.-Z. Zhu, Fluid-structure interaction and band gap analysis of periodic composite liquid-filled pipe, Composite Structures 304 (2023) 116444. doi:10.1016/j.compstruct.2022.116444.
URL http://dx.doi.org/10.1016/j.compstruct.2022.116444

[24] D.-L. Yu, C.-Y. Du, H.-J. Shen, J.-W. Liu, J.-H. Wen, An analysis of structural-acoustic coupling band gaps in a fluid-filled periodic pipe, Chinese Physics Letters 34 (7) (2017) 076202. doi:10.1088/0256-307x/34/7/076202.
URL http://dx.doi.org/10.1088/0256-307X/34/7/076202

[25] H. Shen, J. Wen, D. Yu, X. Wen, The vibrational properties of a periodic composite pipe in 3d space, Journal of Sound and Vibration 328 (1–2) (2009) 57–70. doi:10.1016/j.jsv.2009.07.032.
URL http://dx.doi.org/10.1016/j.jsv.2009.07.032

[26] A. Aladwani, A. Almandeel, M. Nouh, Fluid-structural coupling in metamaterial plates for vibration and noise mitigation in acoustic cavities, International Journal of Mechanical Sciences 152 (2019) 151–166. doi:10.1016/j.ijmecsci.2018.12.048.
URL https://doi.org/10.1016/j.ijmecsci.2018.12.048

[27] Z. Guo, M. Sheng, H. Zeng, M. Wang, Q. Li, Vibro-acoustic performance of a fluid-loaded periodic locally resonant plate, Machines 11 (6) (2023) 590. doi:10.3390/machines11060590.
URL http://dx.doi.org/10.3390/machines11060590

[28] M. Mazzotti, M. Miniaci, I. Bartoli, Band structure analysis of leaky bloch waves in 2d phononic crystal plates, Ultrasonics 74 (2017) 140–143. doi:10.1016/j.ultras.2016.10.006.
URL http://dx.doi.org/10.1016/j.ultras.2016.10.006

[29] R. D. Mindlin, Influence of rotatory inertia and shear on flexural motions of isotropic, elastic plates, Journal of Applied Mechanics 18 (1) (1951) 31–38. doi:10.1115/1.4010217.
URL https://doi.org/10.1115/1.4010217

[30] F. R. M. de Espinosa, E. Jiménez, M. Torres, Ultrasonic band gap in a periodic two-dimensional composite, Physical Review Letters 80 (6) (1998) 1208–1211. doi:10.1103/physrevlett.80.1208.
URL https://doi.org/10.1103/physrevlett.80.1208

[31] S. Shi, C. Chen, D. W. Prather, Plane-wave expansion method for calculating band structure of photonic crystal slabs with perfectly matched layers, Journal of the Optical Society of America A 21 (9) (2004) 1769. doi:10.1364/josaa.21.001769.
URL http://dx.doi.org/10.1364/JOSAA.21.001769

[32] D. Qi, H. Yu, W. Hu, C. He, W. Wu, Y. Ma, Bandgap and wave attenuation mechanisms of innovative reentrant and anti-chiral hybrid auxetic metastructure, Extreme Mechanics Letters 28 (2019) 58–68. doi:10.1016/j.eml.2019.02.005.
URL https://doi.org/10.1016/j.eml.2019.02.005

[33] D. Krattiger, M. I. Hussein, Generalized bloch mode synthesis for accelerated calculation of elastic band structures, Journal of Computational Physics 357 (2018) 183–205.

doi:10.1016/j.jcp.2017.12.016.
URL https://doi.org/10.1016/j.jcp.2017.12.016

[34] W. Ding, T. Chen, C. Chen, D. Chronopoulos, B. Assouar, Y. Wen, J. Zhu, Description of bandgaps opening in chiral phononic crystals by analogy with thomson scattering, New Journal of Physics 25 (10) (2023) 103001. doi:10.1088/1367-2630/acfc5e.
URL http://dx.doi.org/10.1088/1367-2630/acfc5e

[35] W. Pan, G. Tang, J. Tang, Evaluation of uncertainty effects to band gap behavior of circuitry-integrated piezoelectric metamaterial using order-reduced analysis, Journal of Intelligent Material Systems and Structures 29 (12) (2018) 2677–2692. doi:10.1177/1045389x18778359.
URL http://dx.doi.org/10.1177/1045389X18778359

[36] T. Ren, C. Liu, F. Li, C. Zhang, Active tunability of band gaps for a novel elastic metamaterial plate, Acta Mechanica 231 (10) (2020) 4035–4053. doi:10.1007/s00707-020-02728-1.
URL http://dx.doi.org/10.1007/s00707-020-02728-1

[37] C. Kittel, Introduction to solid state physics, John Wiley & sons, inc, 1996.

[38] F. Bloch, Über die quantenmechanik der elektronen in kristallgittern (on the quantum mechanics of electrons in crystal lattices), Zeitschrift für physik 52 (7-8) (1929) 555–600.

[39] W. Setyawan, S. Curtarolo, High-throughput electronic band structure calculations: Challenges and tools, Computational Materials Science 49 (2) (2010) 299–312. doi:10.1016/j.commatsci.2010.05.010.
URL http://dx.doi.org/10.1016/j.commatsci.2010.05.010